Master's Thesis of Climate Studies

Comparison of Onshore and Offshore Boundary Layers in the HARMONIE Model for Wind Energy Purposes

Wageningen University

Meteorology and Air Quality

Author:
Emily Fennell

Supervisors:
Dr. Ir. Gert-Jan Steeneveld
PhD Peter Kalverla

May 16, 2018

MSc Thesis Meteorology and Air Quality, Wageningen University

Title:	Comparison of Onshore and Offshore Boundary Layers in the HARMONIE Model for Wind Energy Purposes
Date:	May 16^{th}, 2018
Author:	Emily Fennell
MSc Supervisors:	Dr. Ir. Gert-Jan Steeneveld PhD Peter Kalverla
Assessment committee:	Dr. Ir. Gert-Jan Steeneveld PhD Peter Kalverla Prof.Dr. Bert Holtslag

Abstract

Harvesting offshore wind is essential to maximise wind energy yields and reach EU renewable energy targets of 20% by 2020. Correctly downscaling wind speed at hub height is crucial as it determines the lifetime and energy production of the wind turbine. Currently there is a deficiency in the validation of how models interpret wind at hub height. Additionally, offshore boundary layer understanding is still lacking due to lack of observations. To address these knowledge gaps, the objective of this paper is to present a comparison of the climatologically observed variables between onshore and offshore boundary layers, alongside a statistical evaluation of the wind and other thermodynamic variables as represented by the mesoscale meteorological model HARMONIE. This study uses observations from two unique meteorological masts, comparing model output, – wind speed, direction, potential temperature and specific humidity, – with offshore observations from the IJmuiden meteomast located 85 km off the coast of the Netherlands, with onshore observations from the Cabauw tower located in the west of the Netherlands, from 2012 through 2014.

Wind offshore is generally more uniform and stable due to homogeneous conditions found over the sea. The accuracy of the model not only differs between offshore and onshore settings, but also varies in altitudes. Generally, the results for both onshore and offshore wind speed imply that the model performance for wind is more precise closer to the surface (RMSE of 1.3 m s^{-1} onshore, 1.9 m s^{-1} offshore) than at higher altitudes (RMSE of 2 m s^{-1} onshore, 2.3 m s^{-1} offshore), whereas both potential temperature and specific humidity are better reproduced at higher altitudes. Furthermore, potential temperature and specific humidity appear to be represented much more adequately offshore (RMSE 0.6 K and 1.2 g kg^{-1} offshore, 0.8 K and 1.7 g kg^{-1} onshore). It is apparent that the overall bias for wind speed is rather small (-0.12 $-$ 0.1 m s^{-1}), whereas the scatter/RMSE remains more substantial (1.2 $-$ 2.3 m s^{-1}).

Contents

List of Figures

List of Tables

1 Introduction

Renewable energies are essential to tackle climate change and mitigate greenhouse gas emissions. Roughly 34% of electricity needs to be generated from renewable energies as opposed to fossil fuels, so that we achieve a reduction of 85-90% in emissions by 2050 (Rodrigues et al., 2015). Wind energy is a renowned, competitive and sustainable way to achieve the European Union's (EU) renewable energy target of 20% by 2020 (Rodrigues et al., 2015; Edenhofer et al., 2011; Kaldellis and Kapsali, 2013). According to the plan defined in EU member states' National Renewable Energy Action Plan (NREAP), the EU expected installed capacity of wind power is 209.6 Giga-Watts (GW), – 165.6 GW onshore and 43.9 GW offshore, – by 2020 (González and Lacal-Arántegui, 2016). In 2017, 15.6 GW of wind power capacity was installed in Europe (WindEurope, 2018).

Socio-economic issues such as land availability, aesthetic impacts and noise pollution impact on the suitability of the placement of the turbine. Moreover the reduction in surface winds over land in Northern Europe (Smits et al., 2005) affect the efficiency of the turbine, as turbines require minimum wind speeds of 5.0 m s^{-1} to operate (Sterl et al., 2015). Alternatively, offshore wind parks (OWP's) have become increasingly popular. With a total of 92 OWP's in Europe producing about 3.2 GW of wind power in 2017 (WindEurope, 2018), this is ~5% of the total wind turbines installed in Europe. Offshore wind is stronger due to the reduced friction between the air and sea (Vilà-Guerau de Arellano et al., 2015), with mean winds over the North Sea of 10.2 m s^{-1} at hub height (Kalverla et al., 2017). This provides us with a substantial increase in power yields and efficiency of turbines as wind speed is generally more uniform due to the homogeneous conditions over sea. These OWP's are becoming increasingly located further from the shoreline, thus increasing the depth of the water in which the turbines are situated. Although offshore conditions are more favourable to efficiency and effective wind energy generation, this comes with greater maintenance and installation costs.

One way to reduce these costs is to develop and design wind turbines that optimize the conditions of a given site (Peña et al., 2016). The optimised design requires understanding of wind turbines in the lowest layer of the atmosphere, i.e. the Atmospheric Boundary Layer (ABL). This is the region where temperature, moisture, wind and other properties of the atmosphere are converted from large atmospheric scales to smaller scales that interact with the surface (Vilà-Guerau de Arellano et al., 2015). ABL flow and its interactions with regards to wind turbines are of uttermost importance for optimizing both the design of the turbine and the efficiency of power generation (Porté-Agel et al., 2014). Due to increasing hub heights of turbines it is necessary to investigate the vertical structure of the boundary layer to describe wind speed profiles correctly (Emeis, 2014). As wind turbines hub-heights are increasing in size, they are typically above the surface layer, – forming ~10% of the total boundary layer (Emeis, 2014). The remaining 90% is the Ekman layer in which the coriolis force causes a turning of the wind with height and reduction of vertical wind shear (Emeis, 2014). Therefore, it is necessary to investigate the full ABL conditions for both offshore and onshore boundary layers, observing the interactions between wind, potential temperature and specific humidity. These vary due to different roughness lengths, lack of boundaries that cause friction and differing roles of entrainment. Although these have been studied in detail over land, offshore conditions are less known due to the lack of measurement stations. This introduces our first research question: "How does the observed atmospheric boundary layer vary between onshore and offshore conditions?".

Another essential step in maximising wind energy yields and minimising costs, is successfully forecasting onshore and offshore winds. One Numerical Weather Prediction (NWP) model used for short-range regional forecasts is the HIRLAM-ALADIN Research on Mesoscale Operational National Weather Prediction model in Europe (HARMONIE). This model was established through the combination of the international research program High Resolution Limited Area Model (HIRLAM) formed in 1985, and the Aire Limitee Adaption Dynamique Developpement International (ALADIN) formed in 1991

(Bengtsson et al., 2017). To provide state-of-the-art Numerical Weather Predictions (NWP) for the 26 countries involved, the AROME model has been adapted for common use between these organisations. It is therefore referred to as the HARMONIE-AROME model (Bengtsson et al., 2017). The model has been recently used to produce a continuous 10-year downscaling product. In this study we analyse the output of this run for two locations of the Netherlands, focusing on the diurnal and seasonal cycles from the years 2012 to 2014. This is to address the second research question "Is the output of the HARMONIE model is a valid representation of the wind speed observations of the North Sea and land conditions?".

The objective of this paper is to compare onshore and offshore boundary layer conditions, and to see whether the downscaling product of the HARMONIE model has the ability to represent these climatological conditions for use in the wind energy sector. The remainder of this paper is organised as follows: Section 2 describes the materials and methods which are used in this study. To achieve the goals of this paper, the results and discussion are divided into two parts, each corresponding to the objectives outlined previously. These are presented in Section 3. The overall conclusion is presented in Section 4.

2 Materials and Methods

This chapter begins with an introduction to the data used within this study, the variables that will be investigated and the step-by-step procedure used for this analysis. The study itself is divided into two parts. The first part consists of a climatological comparison, whereby, observations from onshore and offshore boundary-layer conditions are analysed. These observations are then used to evaluate the HARMONIE model.

2.1 Description of Data

To answer the formulated research questions, we utilize three datasets. Onshore observations from the Cabauw Experimental Site for Atmospheric Remote Sensing (CESAR) are used and offshore conditions from the IJmuiden Mast observations are used. These observations are compared to HARMONIE model output for both locations.

Figure 1: Map indicating the locations of IJmuiden Meteorological Mast and Cabauw Tower (Google Earth, 12/02/2018)

2.1.1 Cabauw Tower

The Cabauw tower research facility is located in the west of the Netherlands at 51.971^o N, 4.927^o E in a polder 0.7 m below mean sea level. It features a tower of height 213 m. The dominant wind of the region is south westerly and is unperturbed over an upstream distance of 2 km (Beljaars and Bosveld, 1997).

Figure 2: Cabauw Tower, KNMI (Wikipedia, 2005)

This region was chosen for the study, as it is representative of mid-latitude grasslands, and is a renowned site for boundary layer studies. The surrounding hinterland is used for agricultural purposes. It consists of meadows separated by ditches, some trees and scattered towns. In general, the area remains quite flat, with slight elevation changes of a few meters over 20 km (Van Ulden and Wieringa, 1996). The direct surroundings are free from obstacles of up to 100 m in all directions (Beljaars and Bosveld, 1997). According to Beljaars and Bosveld (1997), the vegetation at the tower is close to 100% all year round, with grass being kept at a constant height of 8 cm.

As mentioned previously the tower is of height 213 m, with measurements of wind and temperature at heights of 10, 20, 40, 80, 140 and 200 m, with an additional temperature measurement at 2 m. Wind direction is measured in three directions (0 degrees, 120 degrees and 240 degrees). All of which are measured as 10-min intervals. Furthermore surface flux measurements are also available, measuring latent, sensible and ground heat flux and net radiation. These are measured at surface level given at 10-min intervals. These observations can be accessed through the CESAR Database: http://www.cesar-database.nl/. For the purpose of this study we look to the 3 years between 2012-2014.

2.1.2 IJmuiden Mast

The Meteorological Mast at IJmuiden (MMIJ) was built in 2011, and situated 85 km off the Dutch coast at $52^o50'89$"N, $3^o26'12$"E. MMIJ was chosen for this study as it provides a unique representation of marine boundary layer compared to that of other offshore masts. The observations from this tower and LiDAR (Light Detection and Radar) are up to 315 m in height (Kalverla et al., 2017). Therefore, MMIJ provides a unique framework to evaluate models.

Figure 3: IJmuiden Meteorological Mast (Poveda and Wouters, Poveda and Wouters)

Wind speed and direction are measured at 27, 58.5, 85, and 92 m and in the same three directions similar to the Cabauw tower. Sensors on booms have been installed to avoid mast shadow. A LIDAR system is used to measure the wind speed above the mast at 90 to 315 m with 9 intervals of 25 m. There are additional sensors to measure air pressure, temperature, rainfall and relative humidity. These data measurements are given as 10-min averages. Standard deviations, and minimum and maximum values are also provided (Poveda and Wouters, Poveda and Wouters; Kalverla et al., 2017). Further details of this data can be found in the instrumentation report by Werkhoven and Verhoef (2012).

2.1.3 The HARMONIE Model

The HARMONIE model is a non-hydrostatic model that is based on fully-compressible Euler Equations, which are formulated following a pressure based sigma coordinate system (Bengtsson et al., 2017). HARMONIE runs on very high spatial and temporal resolution (Van den Brink and Bosveld, 2017), with a grid space of 2.5 km and time step of one minute (Baas et al., 2016). The lateral boundary conditions are used from the ERA-Intrim (Dee et al., 2011).

According to van den Brink and Bosveld (2017), the time series of HARMONIE consists of hourly averaged wind speed, wind direction and standard deviation of wind. Instead of using hydrostatic approximation, – where in many cases severe-weather events are poorly represented, – HARMONIE solves the vertical momentum equation explicitly (van der Brink et al., 2013). The framework that the HARMONIE model utilises can be found in Bengtsson et al. (2017) and Baas et al. (2016). The neutral-unstable length-scales are composed of vertical integrals of stability dependent functions calculated from the bulk Richardson number (Ri_b), thus allowing for the matching of surface layer similarity for near neutral conditions (Bengtsson et al., 2017). The surface physics of the model is simulated by the surface scheme SURFEX, which is composed of various physical features including natural land surface, urbanised areas, lakes, and oceans (Bengtsson et al., 2017). Consequently, this allows for the comparison between offshore and onshore boundary layers.

The HARMONIE dataset used for this study is in itself unique. The model is generally run for short-term forecasts. However, for this study the model is run over a continuous 10-year period, from 2004 to 2014 (developed by Sterl, A., KNMI). The model output is a product of downscaling a course resolution of 80 km from reanalysis data of the ERA-Interim (Dee et al., 2011) to a much more refined area of 2.5 km. The time frame evaluated in this paper is from 2012 to 2014, – i.e. the latter years from this model run, – as this period is thought to have the most significant deviations from the norm as well as corresponding to those of the observations. For this paper we seek to evaluate whether this technique of running the model is valuable in representing the climatology for offshore and onshore winds, alongside other climatological variables.

The variables in the HARMONIE output are specific humidity [kg kg^{-1}], temperature [Kelvin], eastward wind [m s^{-1}], northward wind [m s^{-1}], vertical velocity [m s^{-1}] and turbulent kinetic energy (TKE) [m^2 s^{-2}], all of which are provided every 3 hours, at heights of 10, 20, 40, 60, 80, 100, 150, 200, 500 m. Alongside these variables sea surface temperature [Kelvin], air pressure [Pa], sea level pressure [hPa], and surface roughness for momentum air [m] are given at 2 m every half hour.

2.2 Comparison of Onshore and Offshore Boundary Layer Observations

To gain an insight into the differences between onshore and offshore atmospheric boundary layers (ABLs), the observations from the meteorological masts of Cabauw and IJmuiden were investigated. These will be referred to as onshore and offshore, respectively. The observations are taken for a 3-year period from January 1^{st} 2012 to December 31^{st} 2014. These coincide with the model output.

The variables that are included in this study are wind speed (U), wind direction, potential temperature (θ) and specific humidity (q) (Figure 5(a)), as these relate to the functionality of the turbine. Wind speed [m s^{-1}] and wind direction [°] are directly measured at both stations, whereas potential temperature [K] and specific humidity [g kg^{-1}] need to be calculated for the observational data at Cabauw. These calculations are given in detail in Appendix A.1. To establish the climatological variations at different time scales, the variables were analysed through averaged diurnal and seasonal cycles.

Alongside these variables, the surface fluxes of latent heat (LE) [W m^{-2}] and sensible heat (H) [W m^{-2}] were further investigated. LE and H are available from surface flux measurements at Cabauw. However, these measurements are unavailable for IJmuiden. In a preliminary study, we tried to reconstruct these fluxes from the wind and thermodynamic observations using the bulk Richardson number Ri_b and flux-profile relationships of LE and H for Cabauw. The same theory is then applied to IJmuiden, using the formula:

$$Ri_b = \frac{g}{T_v} \cdot \frac{\Delta\overline{\theta}}{\Delta\overline{u}^2} \cdot \Delta z, \tag{1}$$

where g is the gravitational constant of 9.81 m s^{-2} and $\overline{T_v}$ is the mean virtual potential temperature (Moene and Van Dam, 2014), $\Delta\overline{\theta}$ is difference in the mean potential temperature between the two heights z_1 and z_2, $\Delta\overline{u}$ is the difference in the mean wind speed between z_1 and z_2, and $\Delta z = (z_2 - z_1)$. This method is further deduced in Appendix A.2.

The result of this preliminary investigation (Appendix A.3), proved quantitatively inaccurate for the observations at Cabauw. This may have been as a result of the lack of closure of the Surface Energy Balance (SEB) at Cabauw (Bosveld, 2010; de Roode et al., 2010). In the absence of reliable flux observations and/or estimates we continued to use the calculated Ri_b with the observations at IJmuiden. This method was also used by Sathe (2010),Dörenkämper et al. (2015),Rodrigues et al. (2015) and Kalverla et al. (2018) for offshore conditions.

It is important to keep in mind that the variables from the locations are measured at different heights. For a fair comparison, corresponding heights were selected prior to this evaluation (Figure 4).

2.3 Validation of Model for Onshore and Offshore Conditions

Similar to the observed variables (Section 2.2), the model data was post-processed to obtain a comparable dataset. For the comparison to remain accurate, the 3-year period of the 1^{st} January 2012 to the 31^{st} December 2014 was chosen. The model output is given as a 3-hour output, whereas the observational data was given in 10-minute intervals. For a more comparable result the observations were averaged over three hours as this resulted in a closer solution to that of the model output.

To gain a more accurate evaluation of the model's behaviour the heights were linearly interpolated to produce uniform heights across all data (Figure 4). The heights examined for θ and q are 21 m and 90 m. As the study focus is wind energy applications, wind speed and direction are evaluated in more depth at heights of 27, 100, and 200 m. These heights were chosen as they relate to the standard hub-heights of turbines ranging from small, kilowatt turbines to large, multi-megawatt wind turbines (Engström et al., 2010; Edenhofer et al., 2011; Chen et al., 2013; Lee, Cho, and Lee, Lee et al.). For wind direction analysis, wind speeds of less than 3 m s^{-1} were removed in order to avoid larger uncertainties in wind direction (Shen et al., 2018).

A detailed error statistics report provides a quantitative assessment of the model performance. The statistical evaluation takes place in different stages (Figure 5b). Throughout this process the numerics 1, 2, 3 and 4 refer to the variables of wind speed, wind direction, potential temperature and specific humidity, as seen in Figure 5a. These are compared through the use of plots a, b, c, d, e and f (Figure 5b). These results are then discussed in the perspective of other NWP models. Furthermore, suggestions for future research and improvements to the model are addressed. The first step is to analyse the model's performance against the observations using simple linear regression analysis (graphs a and b). The second step is to evaluate the errors themselves (in the form of bar charts - graph c) using the three statistical measures, namely the mean bias error (MBE), the root mean sqaure error (RMSE) and the standard deviation of the error (σ) (Murphy, 1988; Nurmi, 2003; Draxl et al., 2015):

$$MBE = \frac{1}{n}\sum_{i=1}^{n}\overline{e_i}, \tag{2}$$

$$RMSE = \sqrt{\frac{1}{n}\sum_{i=1}^{n}{e_i}^2}, \tag{3}$$

$$\sigma^2 = RMSE^2 - MBE^2. \tag{4}$$

Here we define the error between the observations and the model as e_i= $model - observations$. The MBE gives the average difference between the model and observations, whereas the RMSE measures the average magnitude of the error (Nurmi, 2003). Through the use of Pythagoras' theorem these relate to σ representing the average spread of the data (Kalverla et al., 2018). All three statistical measurements can be identified through the use of scatter plots, histograms, wind roses and box-plots and so are used in the evaluation of the model's performance. Both the MBE and the RMSE are analysed together to produce a relatively accurate picture of the errors, giving the best overall measures of how reliable the model is for the variables in Figure 5. The third step evaluates the seasonal variability (using box-plots - graph d) of these errors at the two locations for the variables depending on the heights from Figure 4. The last step establishes the σ and the mean of the error (graph e and f) for diurnal and seasonal cycles in order to determine what time of the year the model conflicts with the true values.

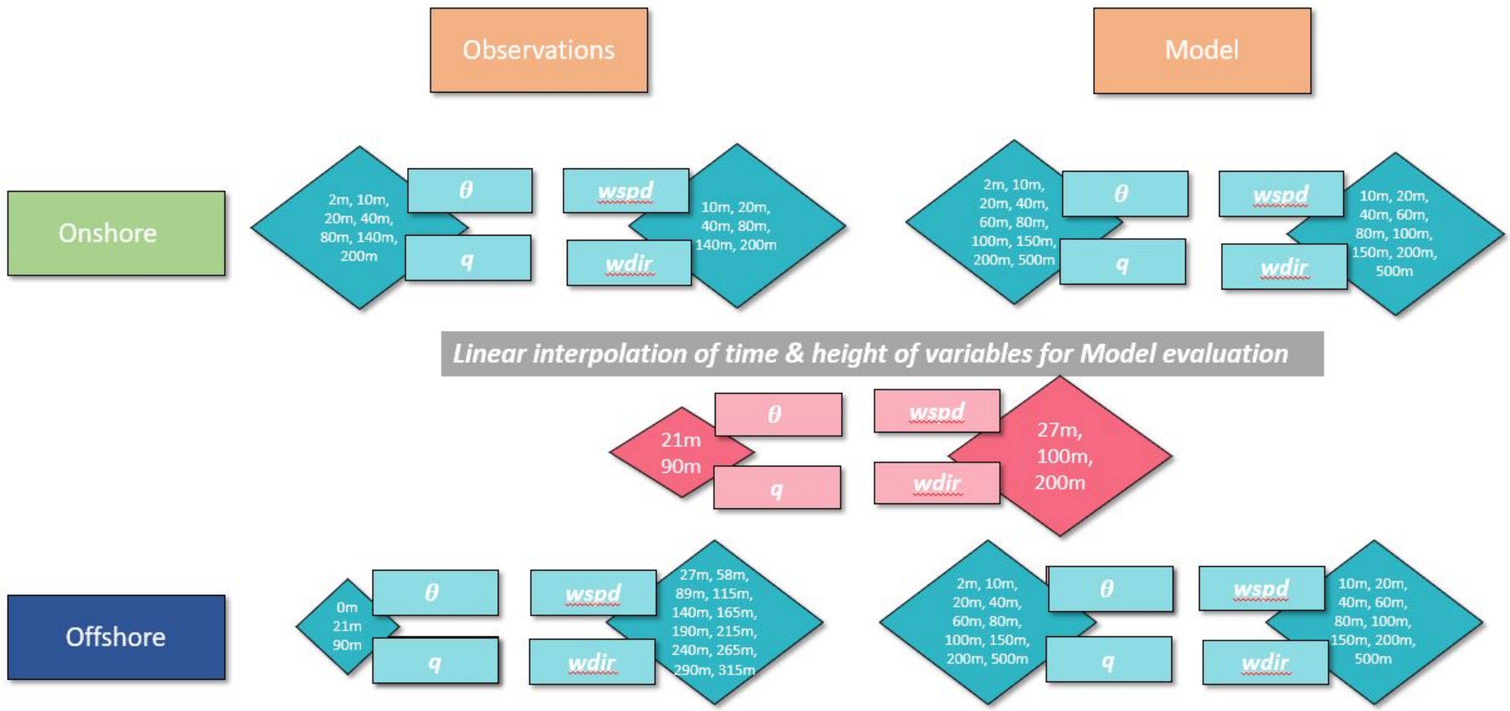

Figure 4: The linear interpolation of height with regards to the model. With different heights between the onshore and offshore observations (on the left) and different heights between the observations and the model (on the right). These are linearly interpolated to produce θ and q at 21 and 90 m, as well as wspd (wind speed) and wdir (wind direction) at 27, 50, 100, 150 and 200 m.

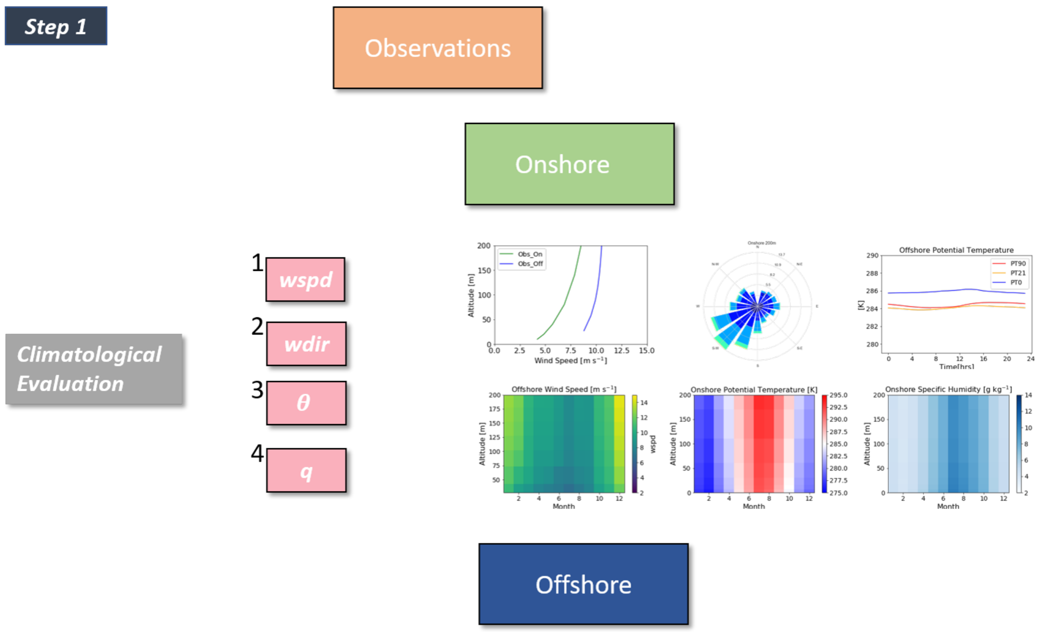

(a) Conceptual diagram for research question 1

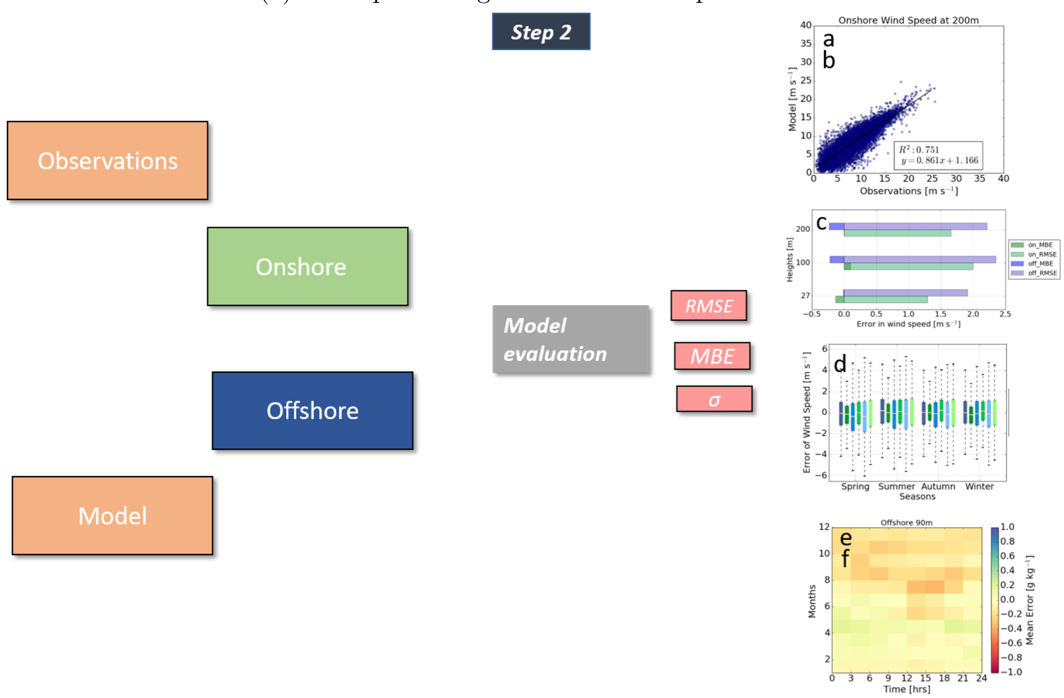

(b) Conceptual diagram for research question 2

Figure 5: Conceptual diagram of the steps taken within this study and example results. **Step 1** 5a: the comparison of onshore and offshore boundary layers by analysing 1 wspd (wind speed), 2 wdir (wind direction), 3 θ (potential temperature), and 4 q (specific humidity). Studying the averaged logarithmic wind profile, wind-roses and looking at seasonal and diurnal variability between onshore and offshore boundary layers. **Step 2** 5b: the statistical evaluation of the model, studying the standard deviation (σ), mean bias error (MBE), root mean square error (RMSE) and mean absolute error (MAE), through the use of scatter plots for onshore (a) and offshore (b) sites, bar-charts (c), box-plots (d) and diurnal & seasonal evaluation of errors for onshore (e) and offshore (f) locations.

3 Results and Discussion

To answer the research questions presented in Section 1 the results and discussion are separated into two studies. Firstly the analysis of the results from the comparative study between the observations is presented, with the discussion of these results and giving a picture of how onshore and offshore boundary layers differ. Following from this the results from the validation of the HARMONIE model are given, accompanied by a discussion of the overall performance of the model. The variables related to this part include wind, potential temperature, specific humidity and surface heat fluxes.

3.1 Comparison of Onshore and Offshore Boundary Layer Observations

3.1.1 Wind

Wind speed determines the amount of energy produced by the wind turbine as well as the point at which the turbine functions, and wind direction is essential for the efficiency and mechanisms related to turbine design. As mentioned previously turbines require a minimum operational wind speed of 5 m s^{-1} (Sterl et al., 2015), and have a cut off point at 25 m s^{-1} (Shen et al., 2018). Therefore they are most valuable in locations where there is constant wind. Thus it is essential to have in-depth knowledge of the locations that fit well within these constraints.

Figure 6a illustrates that the wind speed is indeed greater offshore than onshore, reaching wind speeds of 11 m s^{-1} at higher altitudes, as opposed to onshore results of highs of 8 m s^{-1}. Not only is offshore wind speed larger than onshore, there is also less wind shear, with a steady value from 75 m up to 200 m. Offshore has roughness (z_0) length of 0.0014 m (estimated from this study) whereas onshore z_0 ≈0.03-0.08 m (Verkaik and Holtslag, 2007; Beljaars and Bosveld, 1997). This causes less shear at the surface. Onshore exhibits a more variable increase in wind speed from 4 m s^{-1} at the surface to 9 m s^{-1} at 200 m due to greater friction. Therefore, the wind speed is more heterogeneous with height.

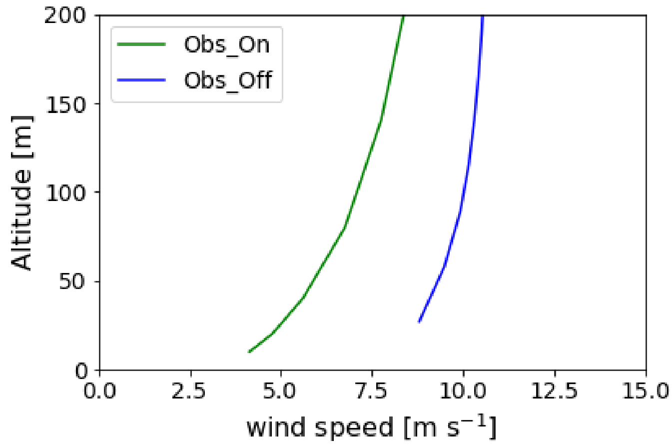

(a) Logarithmic Wind Profile

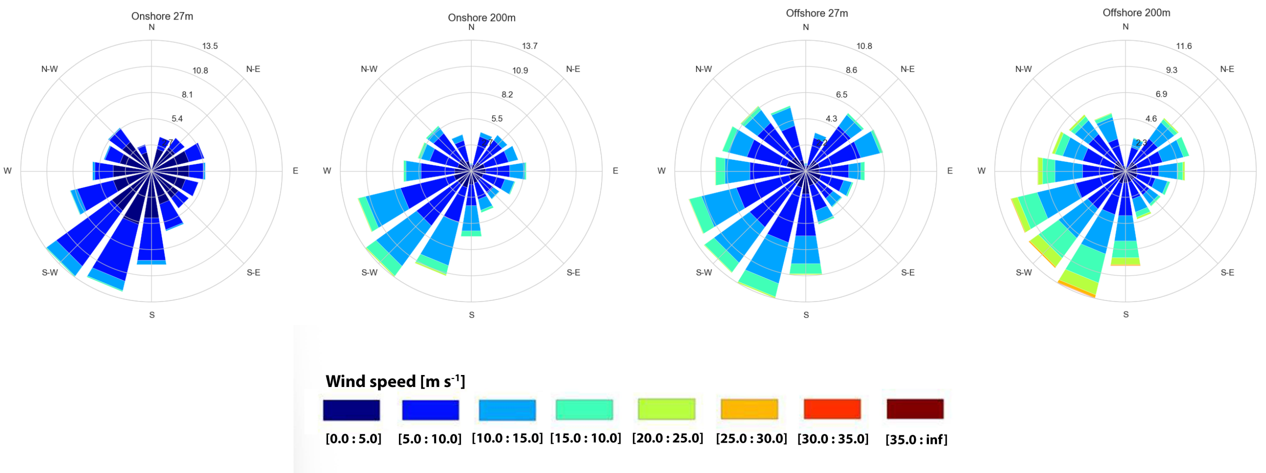

(b) Wind roses

Figure 6: (a) The average logarithmic wind profile from 2012-2014, for Onshore (blue) and Offshore (green). Wind speed [m s^{-1}] on the x-axis and altitude [m] on the y-axis. (b) Wind roses at heights of wind at 27 m and 200 m, onshore and offshore, read from left to right. The wind speed [m s^{-1}] is indicated by the legend below, here N=North, N-E=North-East, E=East, S-E=South-East, S=South, S-W=South-West, W=West, N-W=North-West

This relationship of wind speed with height is also evident in Figure 6b, where winds at 27 and 200 m reach maximum speeds of 15 m s^{-1} and 20 m s^{-1} onshore, and maximum speeds of 20 to 30 m s^{-1} offshore. Here we also see that the dominant wind direction onshore is S-W which is consistent with the prevailing wind of the Netherlands as a result of the Azores high and Icelandic lows. Wind offshore indicates dominant S-S-W wind direction veering with height. The diurnal and seasonal changes in wind speed and direction are further shown in Figures 7 and 8.

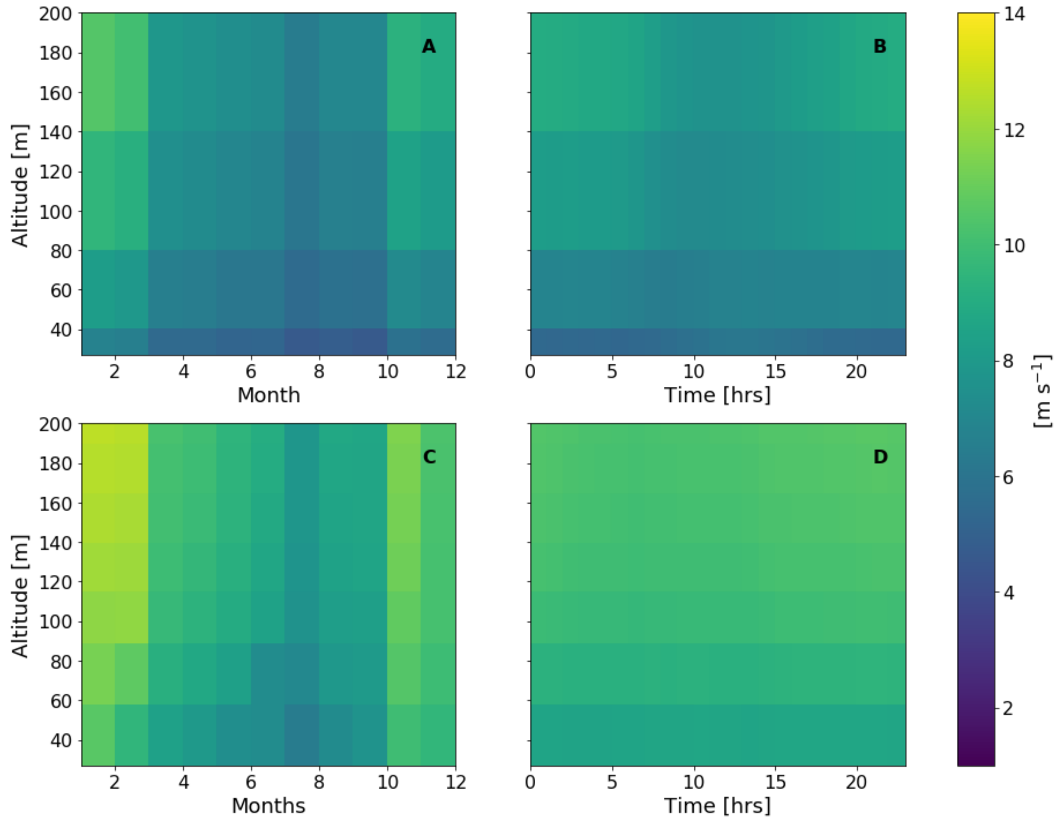

Figure 7: Diurnal and seasonal cycles of wind speed (wspd) [m s^{-1}] indicated by the colour bar. A and B represent onshore settings, with A illustrating average seasonal cycles, and B average diurnal cycle. C and D represent offshore average seasonal and average diurnal cycles respectively.

For both the diurnal and seasonal cycles, there is much more variation in wind speed onshore (Figures 7 A and B), whereas offshore is more consistent in time and height (Figures 7 C and D).

Seasonally, mean wind speed on land reaches maximum values of 11 m s^{-1} in winter and 6 m s^{-1} in summer (Figure 7A). These speeds are found at higher altitudes as surface friction does not play a significant role and the flow is more laminar than the turbulent flow below. Similarly, offshore winds experience this same seasonal cycle. However, winds offshore reach maximum speeds of 14 m s^{-1} in winter months and minimum speeds in summer ($\sim$8 m s^{-1}) (Figure 7C). The increase in wind speeds during winter are due to winter storm surges (Weisse and Von Storch, 2010; Weisse et al., 2012), which are influenced by cyclones over the North Atlantic propagating into the North Sea (Gönnert and Sossidi, 2011).

In Figure 7B, there is a clear diurnal cycle visible onshore, with speeds increasing at 08:00 and slowing at 16:00. This illustrates how incoming short-wave (SW_{in}) and thermal fluxes impact turbulence onshore forcing the boundary layer to grow. Thus the boundary layer experiences greater mixing between the surface and the upper atmosphere. Offshore does not experience this same diurnal cycle (Figure 7D). Here roughness length depends on wave height which can be determined by wind speed (Flamant et al., 2003). Marine boundary layers are relatively more stable and shallow than onshore boundary layers since the surface of the sea is cooler than the air above during spring and summer months (especially at northern latitudes) and H is not as strong offshore. Thus, less mixing occurs between altitudes. Therefore the surface roughness does not play a significant role. However, during storm conditions wave height impacts roughness. However this is not investigated in this study.

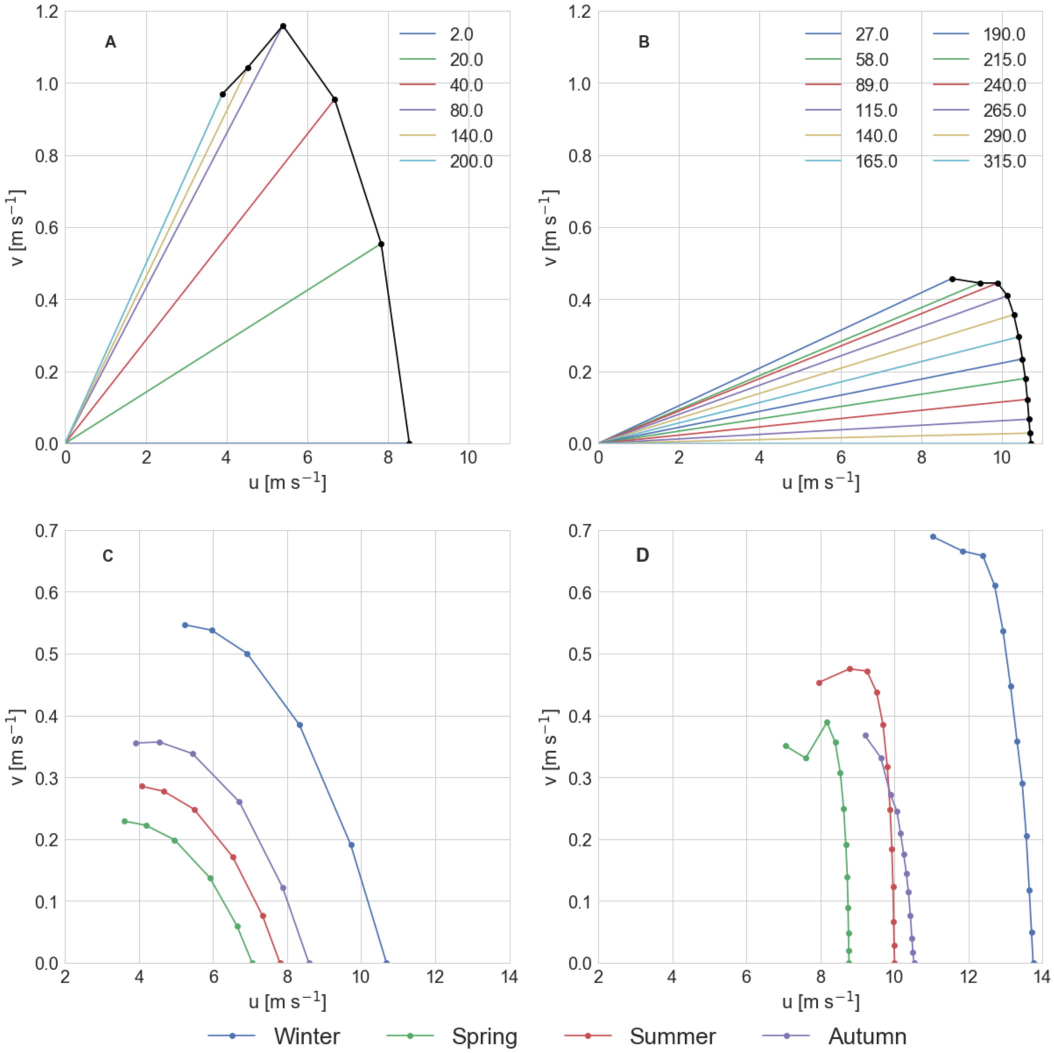

Figure 8: Turning of wind with height, with components zonal (u) and meriodional (v) velocity of wind [m s^{-1}]. A and C represents onshore and B and D represents offshore, with A and B indicating the average turning of wind with height in m. C and D represent the seasonal variation with dots depicting the heights that are indicated in A and B

The Ekman layer spans about 90% of the atmospheric boundary layer (ABL). Figure 7 illustrates that wind speeds tend to increase with height as they move further from the surface layer – where momentum is destroyed by friction, – and closer towards the source of momentum, the free atmosphere (FA). The winds within the Ekman layer adjust their components in order to reach geostrophic balance (Landberg, 2015). This adjustment involves turning of the wind with height (observed in Figures 6b and 8).

Figure 8A illustrates that onshore, as wind speed increases, wind veers with height. Similarly, at low altitudes (27 - 115 m) offshore (Figure 8B), the speed is reduced and the wind veers with height. Wind is once again stronger offshore than onshore, as flow is more laminar offshore with fewer obstacles as opposed to the turbulent flow onshore. These more homogeneous conditions allow for energy to be captured at a more steady rate. The larger frictional force causes a wider angle between the wind and the surface (Hsu, 2013). This is further explored per meteorological season (Figures 8C and D), which coincides with the wind speed results from Figure 7.

The Onshore ABL experiences the same turning effects as before (Figures 8A and C). However, offshore experiences inconsistencies with the change in the direction of wind, – especially during the autumnal months, – when wind speed continues to increase with height and the angle between the surface and higher altitude wind is smaller than that of the other seasonal months. Autumn is the transitional period from stable conditions with calm periods of wind speeds from June to May, to vastly stronger winds and unstable conditions in winter (Stull, 2000). These instabilities are addressed in the next section.

3.1.2 Potential Temperature and Specific Humidity

Many papers have found that wind energy potential may be greater than expected as some studies have not taken into account the stability of the boundary layer (Van den Berg, 2008). Potential temperature is a component that is used in determining the stability of the ABL, and is a key component of the surface energy balance. Specific humidity is directly related to the amount of LE in the SEB and the height of the boundary layer, all of which are influenced and have an impact on the θ. The results for onshore and offshore θ and q are discussed below.

Seasonally θ does not vary substantially with height, but more so over time (Figure 9A), with temperatures in summer of up to 295 K and temperatures in winter ranging from 275-277 K. These variations throughout the year are due to the day-length and the incidence angle of the sun, thereby enhancing and reducing the amount of SW_{in} reaching the surface. Figure 9B indicates that there is a large variation with height diurnally, due to daily fluctuations in the interaction between the surface and the atmosphere. SW_{in} heats up the surface from 07:00 causing the large plume of warm air. These plumes rise from the surface and are transported upwards through the process of convection. This is similar to Figure 7B where the growth and diminishing of the boundary layer is observed at the same time as the heating and cooling onshore.

In both the diurnal and seasonal cycles, θ_0 has a slightly higher θ compared to the air above. This is due to the direct heating of the sun, and the large heat capacity of water (Figure 9E and F). Similar to onshore seasonal cycles, offshore θ at 21 and 90 m return maximum temperatures in July and August and minimum temperatures of $\sim$278 K in winter months. $\theta_{90} > \theta_{21}$ since the conditions over the sea are more stable as warm air remains over the cooler surface. What is striking for offshore conditions is that the sea surface temperature (SST) follows a slight diurnal pattern, with peaking temperatures of 286.93 K at mid-day.

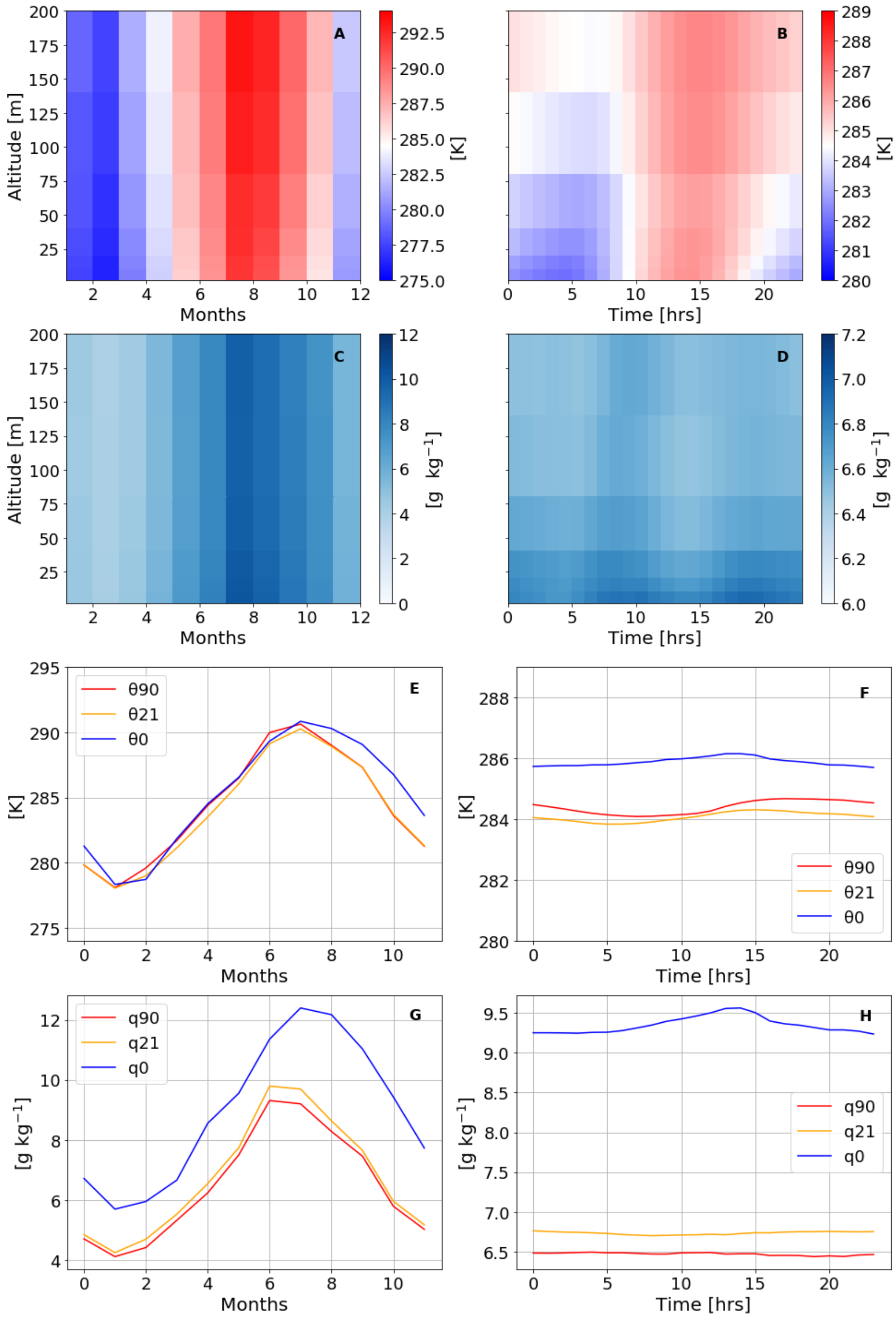

Figure 9: Onshore: A,B,C,D and offshore: E,F,G,H conditions. A & B illustrate onshore potential temperature [Kelvin] and C & D correspond to onshore specific humidity [g kg^{-1}]. The y-axis indicates altitude [m] and the x-axis indicates the time in months or hours. E & F illustrate offshore potential temperature (PT) [Kelvin] and G & H correspond to onshore specific humidity (q) [g kg^{-1}]. The y-axis is the unit, and the x-axis is time in months or hours. Here the blue indicates surface ($\theta 0$,q0), yellow is at 21 m ($\theta 21$,q21) and red is at 90 m ($\theta 90$,q90).

Likewise, onshore specific humidity is greatest in summer (12 g kg^{-1}) and lower in winter ($\sim$4 g kg^{-1}) (Figure 9C) as cold air can hold less moisture than warm air. The greater the amount of energy received from the sun the greater H and LE fluxes, thus increasing the temperature and evaporation at the surface, causing an increase in q_0. This is evident throughout the course of the day (Figure 9D), as the lower layers from 07:00 to 17:00 are more moist when the temperature increases. From noon to 15:00 dry air is entrained from the FA to the surface. This is indicated by a slight increase in wind speed seen in Figure 7B.

Figure 9G shows a peak for q in summer, and a decline towards February. Unsurprisingly q0 has the largest value as the location is closest to a body of water, and the difference between 21 and 90 m is minimal, tending to have a difference of 0.1 g kg^{-1} as q_{21} experiences a greater amount of evaporation. During the average day offshore (Figure 9H), the moisture available at q_0 is $\sim$2.25-2.75 g kg^{-1} damper than higher altitudes. There is however a slight variation in q_0 that corresponds to the slight change in θ_0, – i.e. as θ increases the air becomes saturated and therefore q increases also. As $\theta_{90} > \theta_{21}$, q_{21} may be influenced by both the presence of water below or the direction that the wind is coming from. The seasonal cycles indicate results comparable to both those found for θ and those found onshore.

3.1.3 Vertical Gradients

The Bulk Richardson number and the related variables of $\Delta U, \Delta\theta$ and Δq are analysed, followed by the latent and sensible heat flux, – firstly discussing onshore results and following with the results for offshore.

3.1.3.1 Onshore

Relating to the theory of atmospheric dynamic stability (Appendix A.2), onshore indicates rather mixed conditions as $\mathrm{Ri}_b > 0$ for 55% of observations. To understand these results the changes in U, θ and q have been assessed below.

Wind speed experiences the most substantial differences between 40 and 10 m (Figure 10b.1). ΔU shows a clear diurnal cycle as the difference between the two heights is less during the day (0.75-1 m s^{-1}), and more substantial at night (2 m s^{-1}). The seasonal cycles display large changes in wind speed with height (seen in Figure 7A), where $U_{40m} > U_{10m}$ and ΔU exhibits more stable conditions. $\Delta\theta$ has daytime values of -0.25 K, ($\theta_{40m} < \theta_{10m}$), with this range depleting at night. Seasonal cycles indicate the largest difference in $\Delta\theta$ (1-1.5 K) (Figure 10b.2). Δq follows the same diurnal cycle as that of ΔU and $\Delta\theta$, although having less of a difference between heights during the day (-0.2 g kg^{-1}) (Figure 10b.3). During the day there is more moisture closer to the surface than at 40 m, this is due to dry air entrainment (see Figure 9D) and less moisture at the surface at night. As there are more unstable conditions during summer months, there is a larger $\Delta\theta$ and Δq. These results relate to the measured LE and H fluxes onshore.

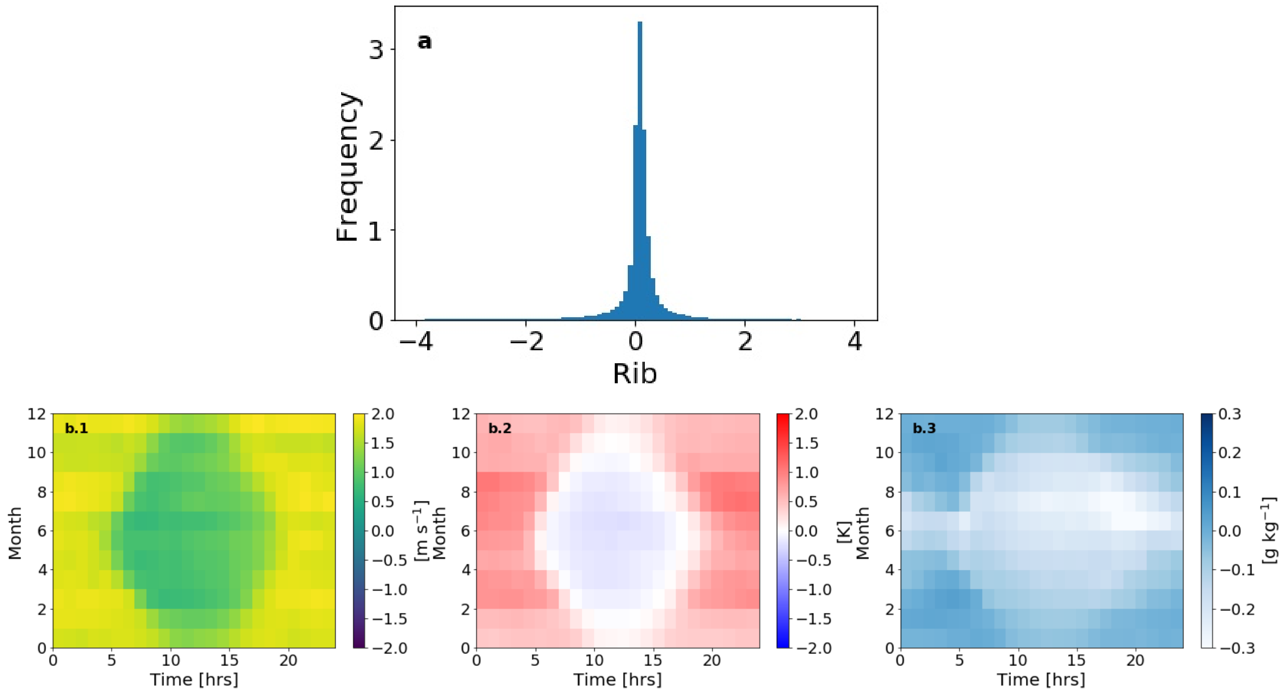

Figure 10: a) Histogram of the calculated Ri_b for onshore conditions, using the theory from Appendix A.2. Graphs b.1-3 show the diurnal (x-axis) and seasonal (y-axis) cycles of the changes in the onshore variables between the heights of 40 and 10 m; b.1 is ΔU which is the change in wind speed [m s^{-}1], b.2 is $\Delta\theta$ which is the change in potential temperature [K] and b.3 is Δq which is the change in specific humidity [g kg^{-1}] between 40 and 10 m.

Figure 11 reveals that the SEB components are influenced and contribute to U, θ and q. The quantitative results are discussed in Appendix A.3. Qualitatively it can be seen that H and θ show the highest relation both seasonally and diurnally. During day time conditions (where $\theta_{40} < \theta_{10}$ in Figure 10) H is highest with maximum values of 80 W m^{-2}. Likewise during unstable conditions in spring/summer months, H is $\sim$10 W m^{-2} greater at more stable conditions during autumnal/winter months. This is similar to the results of LE. Here LE values range from 150-$\sim$300 W m^{-2} during the day. This is enhanced where the air at 10 m is more saturated then the air above (Figure 10b.3).

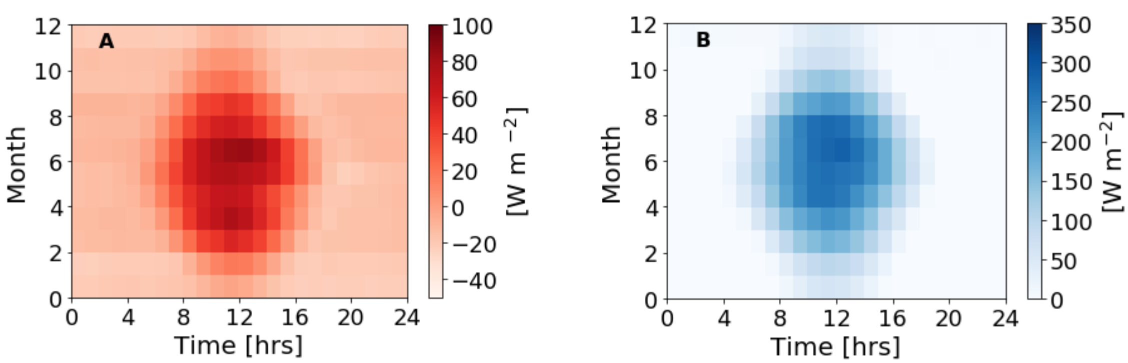

Figure 11: Diurnal (x-axis) and seasonal (y-axis) cycles of observational measurements of (A) sensible heat flux (H) and (B) latent heat flux (LE) in W m^2 at Cabauw.

From this study, we can conclude that it is best to look at the gradients of ΔU, $\Delta\theta$ and Δq to investigate whether this theory stands for offshore conditions (Section 3.1.3.2).

3.1.3.2 Offshore

Heights between 21 and 90 m were chosen for offshore conditions. Previous results have strongly supported the fact that offshore conditions experience a more stable boundary layer. However, $\mathrm{Ri}_b > 0$ (stable conditions) for 43% of observations (Figure 12A). This is lower than those found onshore. Once again ΔU, $\Delta\theta$ and Δq are assessed.

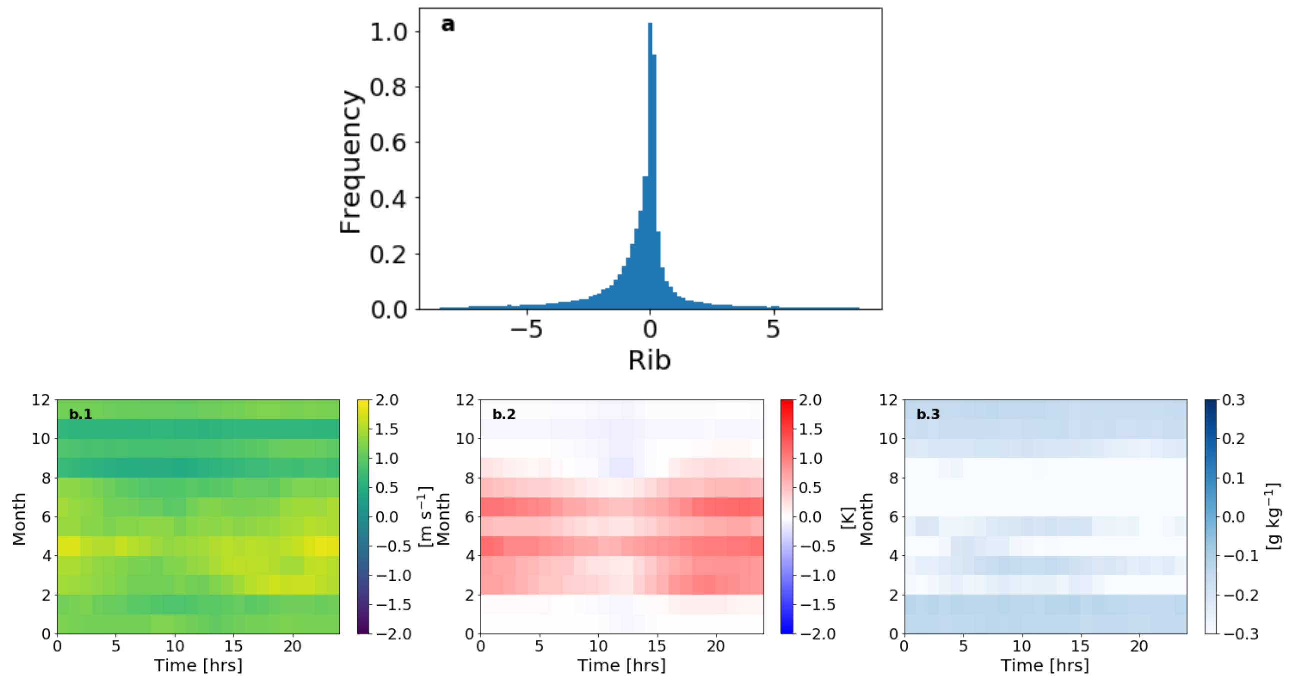

Figure 12: a) Histogram of the calculated Ri_b for offshore conditions, using the theory shown in Appendix A.2. Figures b.1-3 show the diurnal (x-axis) and seasonal (y-axis) cycles of the changes in the offshore variables between the heights of 23.5 and 89 m. Where b.1 is ΔU which is the change in wind speed [m s^-1], b.2 is $\Delta\theta$ which is the change in potential temperature [K] and b.3 is Δq which is the change in specific humidity [g kg^{-1}] between 23.5 and 89 m.

The Ri_b is strongly influenced by θ, where $\mathrm{Ri}_b < 0$, $\Delta\theta < 0$. Once more we see little variability over the course of the day (Figure 10b). During spring/summer $\Delta\theta$ and ΔU are stronger (positive) indicating that the boundary layer is more stably stratified in these months. However, $\Delta q =\sim 0.3$ g kg^{-1} during the summer indicating that the air is drier and thus less stable. Offshore $\Delta q < 0$ for most cases (Figure 10b.3). This explains why Ri_b indicates less stable conditions offshore than onshore.

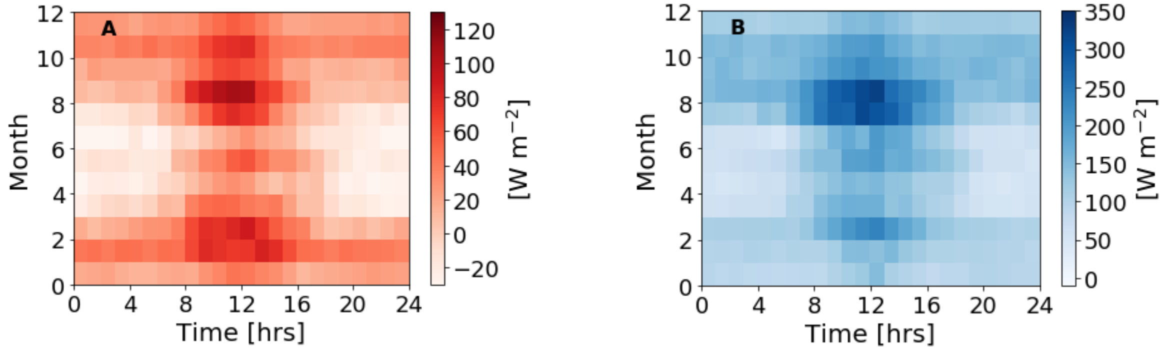

Figure 13: Diurnal (x-axis) and seasonal (y-axis) cycles of the calculated (A) sensible heat flux [W m^{-2}] and (B) latent heat flux [W m^{-2}] for offshore, using the theory from Appendix A.2.

Finally these results are used to estimate the H and LE (Figure 13). Although the vertical gradients indicated little variation diurnally, both H and LE show a slight diurnal cycle, with a greater amount of energy released from the surface during day time conditions. Offshore locations generally experience large evaporation processes due to the large body of water below. This is seen during midday conditions where LE reaches ~300 W m^{-2}. LE is greatest in autumn months. Similarly H experiences the same diurnal and seasonal cycle, with maximum values of 120 W m^{-2}. Autumn is associated with more unstable conditions (Kalverla et al., 2017).

With regards to stability, there is a much larger range of Ri_b offshore than onshore. The greater instability observed offshore is a result of a lack in diurnal cycles with height and smaller ΔU and Δq. The onshore site seems to experience more stable conditions with wind speed having the most significant influence on Ri_b.

3.1.4 Discussion of the Observations

In the comparison of onshore and offshore conditions, it is evident that wind is indeed higher over sea than over land, reaching maximum mean wind speeds of 13 m s^{-2} offshore as opposed to wind speeds of 8 m s^{-2} onshore. This is a result of the stronger attenuation wind onshore due to the higher surface roughness (as mentioned in Section 3.1). According to our findings, potential temperature was highest over land with daily temperatures reaching 289 K as opposed to ∼285 K offshore. Although there was more moisture at the surface over the North Sea due to the fact that it is a large body of water, specific humidity was greater onshore with maximum moisture of 7 g kg^{-1} than offshore at 21 and 90 m (6.7 g kg^{-1}) implying that mixing onshore is much more effective.

These results correspond to the results found in Hsu (1986) and Hsu (1980). Although Hsu (1980) study is over the U.S, he found that onshore wind represented 63% mean wind speed of offshore conditions. Our study indicates that wind at Cabauw is about 65%. Likewise, Hsu (1986) found that the ratio between wind speed over land and over sea is 1.54.

We found that 55% of the time the boundary layer onshore is stable (Figure 10). However in a study by Van den Berg (2008), he found that the atmosphere at Cabauw is stable for 43% of the time with most daytime conditions being unstable, similar to our results in Figure 10b.2. These instabilities are caused by the dominating ground heating (Figure 9B). As the surface temperature increases the stability decreases and turbulent mixing becomes the dominating effect (Figure 10b.1). Entrainment plays a significant role in the evolution of the onshore boundary layer (Figure 9D). Rapidly growing wind speeds favour conditions of maximum entrainment seen in Figure 7 A and B and Figure 9 C and D. However, significant changes in the climatic conditions with regards to potential temperature and specific humidity can impact on the performance and functionality of the airfoil/blade/rotor of the turbine (Yu and Yan, 2017). High amounts of moisture can cause rusting and degradation to the materials of the turbine. This is an issue related to the placement of wind turbines offshore, and is also related to onshore conditions as Cabauw experiences relatively large quantities of moisture, − LE is ∼250 W m^{-2} during the day (Figure 11B), − (Steeneveld et al., 2005).

In contrast to the results found onshore, the offshore boundary layer exhibits little variation diurnally as sea water and air temperature above is relatively constant (Figure 9F). Thus the stability mixing over the sea is relatively small (Coelingh et al., 1996). Similar to the results found by Coelingh et al. (1996) and Van Wijk et al. (1990), the North Sea exhibits relatively unstable conditions (57% of observations as seen in Figure 12A) as the sea surface temperature is warmer than the air above. Seasonal variations are more prominent offshore with maximum wind speeds in winter (Figures 7C) due to the occurrence of storms and unstable conditions. Spring and Summer on the other hand are dominated by stable conditions especially at higher altitudes (Figures 9 E and F). Seemingly, thermal advection of heat has a significant impact on the state of the marine boundary layer (Section 3.1.3.2).

It is important to note that the observations at these meteorological stations are not perfect. There are gaps in the observational data at Cabauw due to instrument failure, maintenance issues and difficulties in data communication (Beljaars and Bosveld, 1997). These failures are also evident at the IJmuiden mast. Furthermore, we did not take into account the surface conditions such as wave height or the errors related to the measurement of surface temperature.

In the following section, we investigate whether the HARMONIE model adequately captures the contrasting boundary-layer conditions for onshore and offshore conditions.

3.2 Validation of Model for Onshore and Offshore Conditions

3.2.1 Wind

When considering the design of wind turbines it is necessary for the model to represent the components of the wind to a sufficiently high degree. Here the errors in wind speed and wind direction are analysed in depth (described in Section 2.3).

Figure 14 indicates that the HARMONIE model behaves relatively well with regards to wind speed. The correlation coefficient $R^2 \approx 0.8$ for both onshore (Figure 14a.1) and offshore (Figure 14b.1). The error itself becomes much more narrow as wind speed increases giving a tear-drop-like pattern at all heights. This becomes much more apparent offshore, as winds are much faster due to the lack of obstacles and lower roughness lengths (Section 3.1.1).

Figure 14c.1 shows that between all heights (27, 100 and 200 m) RMSE values range between $1.3 - 2$ m s^{-1} onshore and $1.9 - 2.3$ m s^{-1} offshore. For both locations, wind speed is better represented at heights closest to the surface (27 m) than at increasing altitudes. One could expect that the error of the model would increase as we move further from the surface. However, this is not the case. The RMSE of wind at 100 m is greater as the model deviates from the standard logarithmic profile. This is possibly due to the occurrence of low level jets (Henderson et al., 2003; Storm et al., 2009). The model may be unable to recognise and interpret these events. The MBE gives a slightly different perspective. It is important to note is that the bias is relatively small for all locations and all heights (ranging between -0.2 and +0.1 m s^{-1}). However, in analysing each location in depth, there is a larger uncertainty offshore as MBE indicates that there is an underestimation in the results. As seen from the RMSE, offshore wind speed at 27 m is represented quite well (MBE of -0.01 m s^{-1}). In contrast, onshore conditions show a different finding. Wind speeds are underestimated at 27 m (MBE of -0.13 m s^{-1}), and overestimated at 100 m (MBE of 0.1 m s^{-1}). These results are interesting because, while the overall error statistics are smaller offshore, the variation of error with altitude is larger.

Both the observations and the model indicate that on average wind speed varies from season to season (Figures 7 A and C and 14d.1). The greatest variability occurs in the spring and summer months when the wind speed is increasing and reaching maximum strengths. Once again it is evident that the model tends to produce more accurate results onshore. In spring and summer months median values of the error in wind speed offshore are close to 0 m s^{-1} especially at 200 m. Throughout all seasons, offshore wind speed tends to be underestimated for 100 and 200 m and are better represented at 27 m. This corresponds to the results from Figure 14c.1.

In summary as wind speed increases the error becomes more narrow (Figures 14a.1, b.1). For onshore conditions in winter months the error is $\sim$0.7 m s^{-1} and the spread is relatively small (Figure 14d.1). Both the mean error and the standard deviation of the error increase with increasing altitude (for onshore and offshore sites). From these results we can conclude that HARMONIE simulates wind speed better at lower altitudes. Overall the model forecasts more accurate wind speed results onshore.

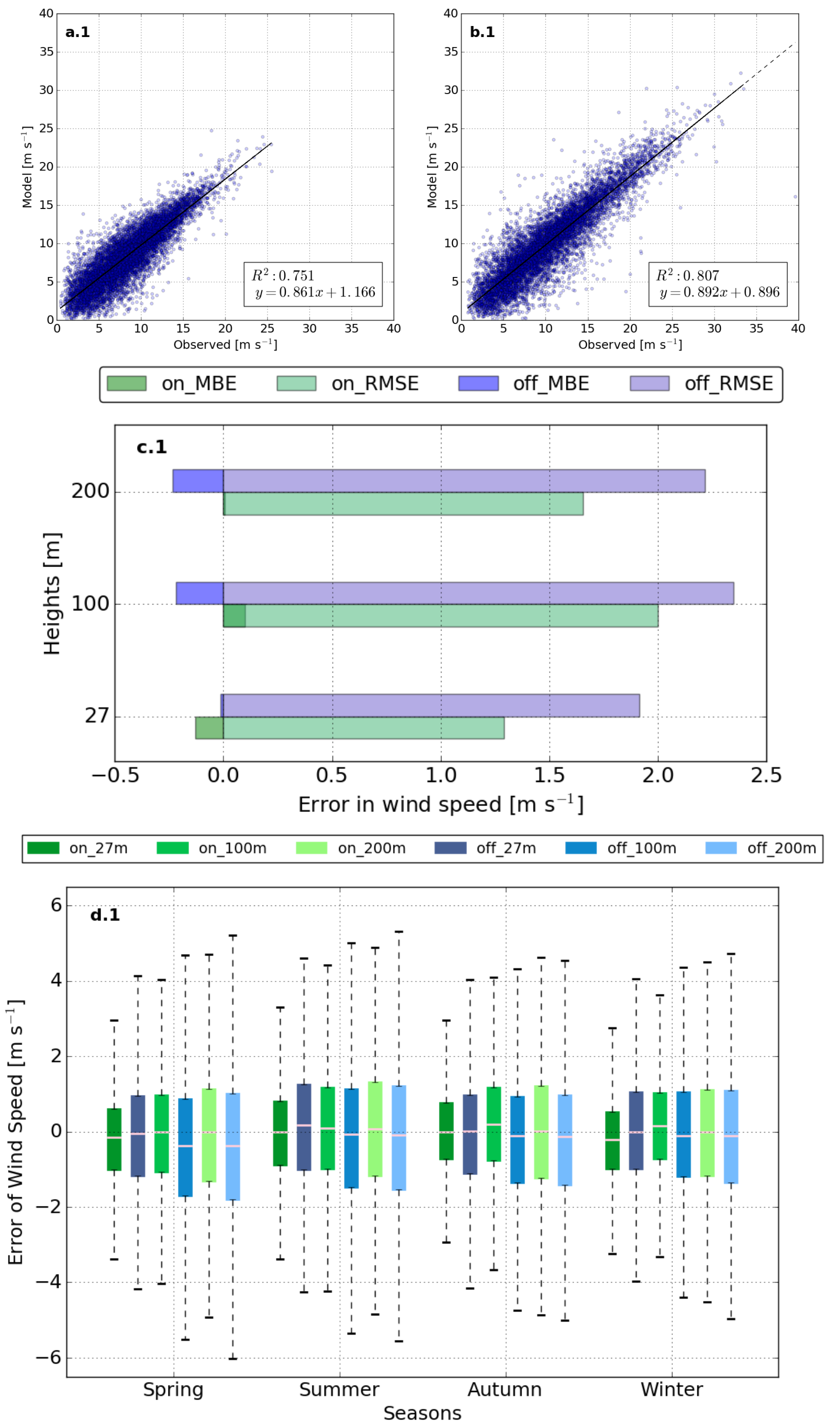

Figure 14: Statistical analysis of wind speed(1) [m s^{-1}]. Scatter plots (a and b) of wind speed at 200 m for onshore (a.1) and offshore (b.1) with the observations (x-axis) compared with the model output (y-axis). Bar-chart (c.1) with the bias (MBE) and the root mean square error (RMSE) (x-axis), for onshore (green) and offshore (blue) at heights (y-axis) 27, 100 and 200 m. The darker shade indicates the bias and the pale colour indicates the RMSE. Box-plot (d.1) of the seasonal errors of onshore (green) and offshore (blue) for heights 27, 100, 200 m, the lighter the shade of the colour the higher the altitude. The pink line indicates the median. The seasons are determined by the meteorlogical seasons: Spring = March, April, May, Summer = June, July August, Autumn = September, October, November, and Winter = December, January, February.

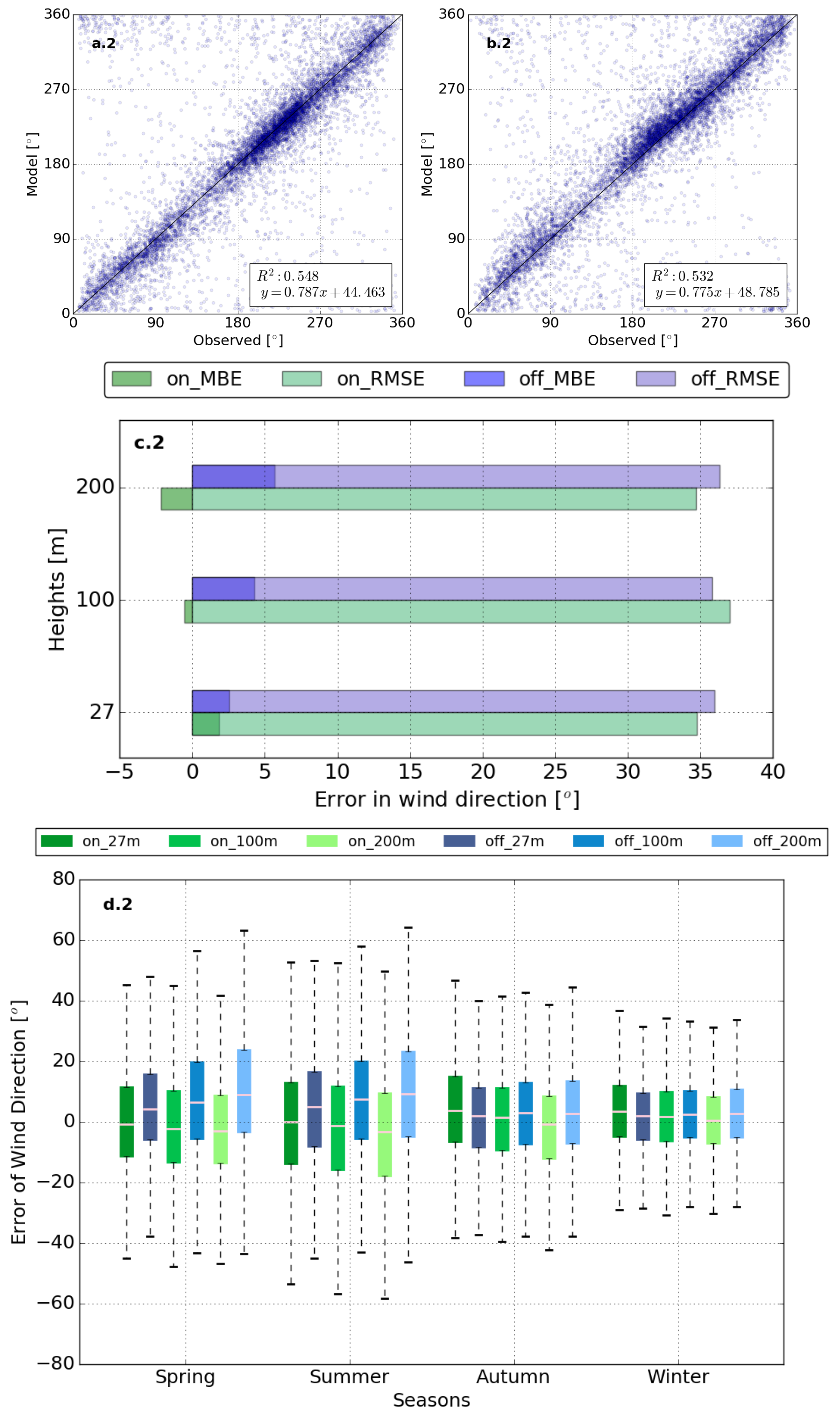

Figure 15: Statistical analysis of wind direction(1) [°]. Scatter plots (a and b) of wind direction at 200 m for onshore (a.2) and offshore (b.2) with the observations (x-axis) compared with the model output (y-axis), the black line indicates the 1:1 line. Bar-chart (c.2) with the bias (MBE) and the root mean square error (RMSE) (x-axis), for onshore (green) and offshore (blue) at heights (y-axis) 27, 100 and 200 m. The darker shade indicates the bias and the pale colour indicates the RMSE. Box-plot (d.2) of the seasonal errors of onshore (green) and offshore (blue) for heights 27, 100, 200 m, the lighter the shade of the colour the higher the altitude. The pink line indicates the median. The seasons are determined by the meteorlogical seasons: Spring = MAM, Summer = JJA, Autumn = SON, and Winter = DJF.

Unlike wind speed, wind direction is not necessarily represented "well" by the model. R^2 ranges between $0.56 - 0.6$ (Figure 15a.2, b.2). It is important to note that these results are slightly skewed due to the relationship between 0° and 360°. The pattern in wind direction is the same at both locations and at all heights. In general the trend is positive for both onshore and offshore conditions. However, wind direction has a better fit offshore between 180° and 270° with most scatter above the line (Figure 15b.2).

Figure 15c.2 indicates that onshore wind direction is slightly better represented than offshore. Although these errors are relatively large, RMSE values are 2° smaller onshore than offshore. This indicates that the model fits better with the results from onshore observation which are similar to the results of wind speed (Figure 14c.1). Offshore wind directions are overestimated by the model, slightly increasing in inaccuracy with an increase in elevation (RMSE 35.96° at 27 m to 36.31° at 200 m). The onshore bias tends to differ between altitudes. The model overestimates wind direction at 27 m (1.8°), and underestimates at 100 and 200 m (-0.6 and -2.3° respectively). At 100 m the model exhibits more accurate results for offshore conditions than onshore, with a slightly undervalued bias onshore. The model represents too large a wind direction offshore. An hypothesis for this is the inaccurate representation of surface drag which is dependent on the wind speed reflected by HARMONIE. The model also fails to reproduce accurate offshore wind speed (Figure 14c.1) which further influences the surface roughness (van der Brink et al., 2013), impacting drag and therefore wind direction.

The error in wind direction has the smallest deviation in the winter months (Figure 15d.2). Once more, wind direction onshore is better interpreted by the model, with median errors closest to zero. However, generally the model overestimates wind direction, increasing with height in spring/summer, and decreasing in autumn. In winter the error is relatively the same, – per location and per height, – slightly overestimating the true value. This could be a result of the models inability to forecast warm advection therefore reducing the ability to predict the veering of wind (Brown et al., 2005).

Although wind direction changes (slightly) with height in all locations (see Figure 8), the model does not necessarily take this into account. The errors offshore have more or less the same results when analysing the diurnal and seasonal cycles (See Table C.1 Appendix C). Despite the change in spread of error (Figure 15d.2), wind direction onshore does in fact provide a better fit to the observations. However, errors at both locations still seem to be relatively large.

To clarify which mechanisms influence the errors seen in wind speed and direction, errors of potential temperature and specific humidity within the model are discussed below. In Section 3.1.2 and 3.1.3 we noted how θ and q can influence the stability and structure of the boundary layer. Therefore, it was deemed a requirement to assess their performance within the HARMONIE model.

3.2.2 Potential Temperature and Specific Humidity

The model represents θ relatively well against observations at 21 m (Figure 16 a.3 and b.3). There is no significant deviation from the scatter between the heights of 21 and 90 m with values ranging between $0.93 - 0.95$ R^2. There is a large spread onshore (Figure 16a.3), most likely due to the greater variations in the interactions between the surface and the atmosphere (discussed in Section 3.1.2). However the pattern remains relatively the same with temperatures congregated between 270-295 K. On the other hand, there is a slight difference between the two heights offshore (Figure 16c.3). Close to the surface temperatures are cooler (265-295 K) than at 90 m (265-304 K). The greater the temperature the greater the deviation from the line. This could be as a result of the model being unable to represent the gradual increase and/or decrease in temperatures found in the observations (Figure 9E, F).

When examining these two locations in more detail, it is evident that the model behaves better offshore than onshore (Figure 16c.3). RMSE $<$ 1.4 K offshore and RMSE $<$ 1.6 K onshore. In addition, the MBE indicates that the model underestimates θ especially onshore (-0.7 K), concluding that HARMONIE represents offshore θ better than onshore.

The spread in error is further assessed through seasonal errors (Figure 16d.3). Overall it is apparent that onshore θ is undervalued by the model at all heights, and throughout all seasons. Summer exhibits the highest depreciation with mean values of -1 K at 21 m and -0.8 K at 90 m. On the other hand, the model overestimates offshore conditions during summer months, with highest temperatures reaching up to 295 K onshore and 292 K offshore. As temperature increases, the model's representation of onshore conditions becomes less reliable, whereas offshore conditions seem to be more promising. This is further addressed through diurnal and seasonal cycles (Figure 17 e.3 and f.3).

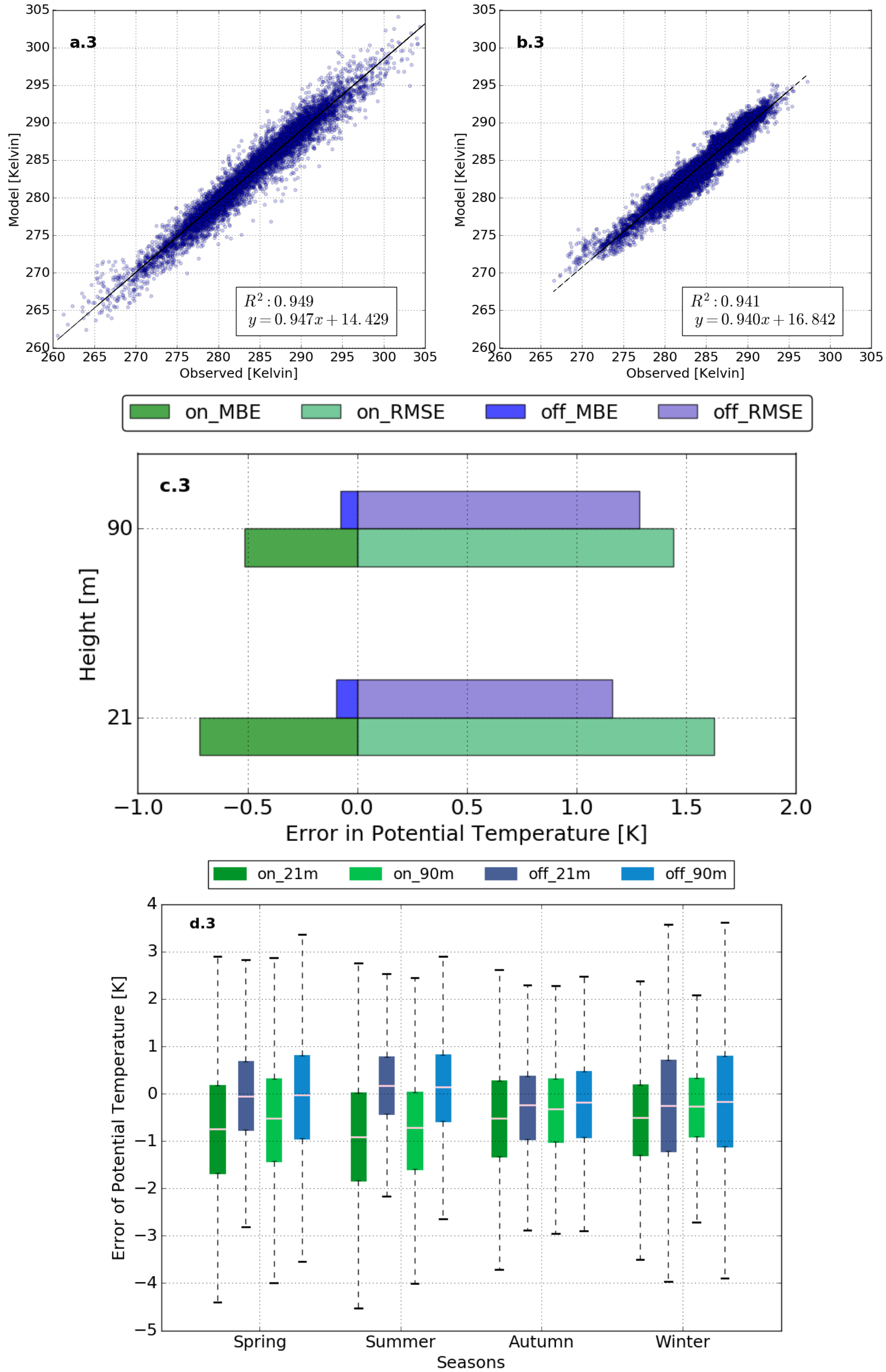

Figure 16: Statistical analysis of potential temperature [Kelvin]. Scatter plots (a and b) of θ at 21 m for onshore (a.3) and offshore (b.3) with the observations (x-axis) compared with the model output (y-axis). Bar-chart (c.3) with the bias (MBE) and the root mean square error (RMSE) (x-axis), for onshore (green) and offshore (blue) at heights (y-axis) 21 and 90 m. The darker shade indicates the bias and the pale colour indicates the RMSE. Box-plot (d.3) of the seasonal errors of onshore (green) and offshore (blue) for heights 21 and 90 m, the lighter the shade of the colour the higher the altitude. The pink line indicates the median. The seasons are determined by the meteorlogical seasons: Spring = MAM, Summer = JJA, Autumn = SON, and Winter = DJF.

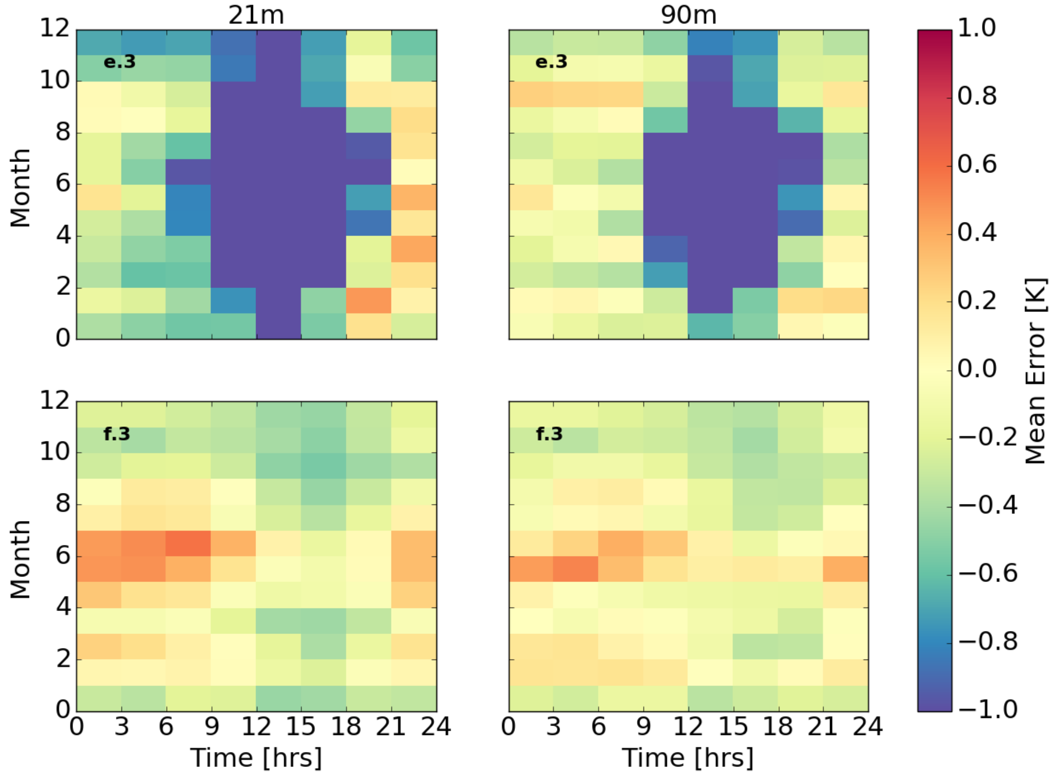

Figure 17: Average diurnal (x-axis) and seasonal (y-axis) cycles of the mean error in potential temperature [K] at 21 and 90 m onshore (e.3) and offshore (f.3). The error ranges between -1 (blue) and 1 (red), where blue indicates an underestimation of θ, and red indicates an overestimation of θ.

Figure 17 indicates that seasonally where temperature are highest (i.e. in summer months), the model overestimates the temperature with mean error of 0.8 K, and reflects slightly cooler temperatures in winter months. Therefore, one could assume that when the temperature increases the model overestimates the temperature slightly. However, this is not the case. In the diurnal cycle of θ, the plume observed onshore in Figure 9B is underestimated by the model (Figures 17e.3), with a mean error of -1 K. A slight underestimation of θ is also evident offshore (f.3 at 21 m) between 15:00 and 18:00 (-0.3 K). These results may be due to the underestimation of sensible heat fluxes within the model (see discussion of Figure 20).

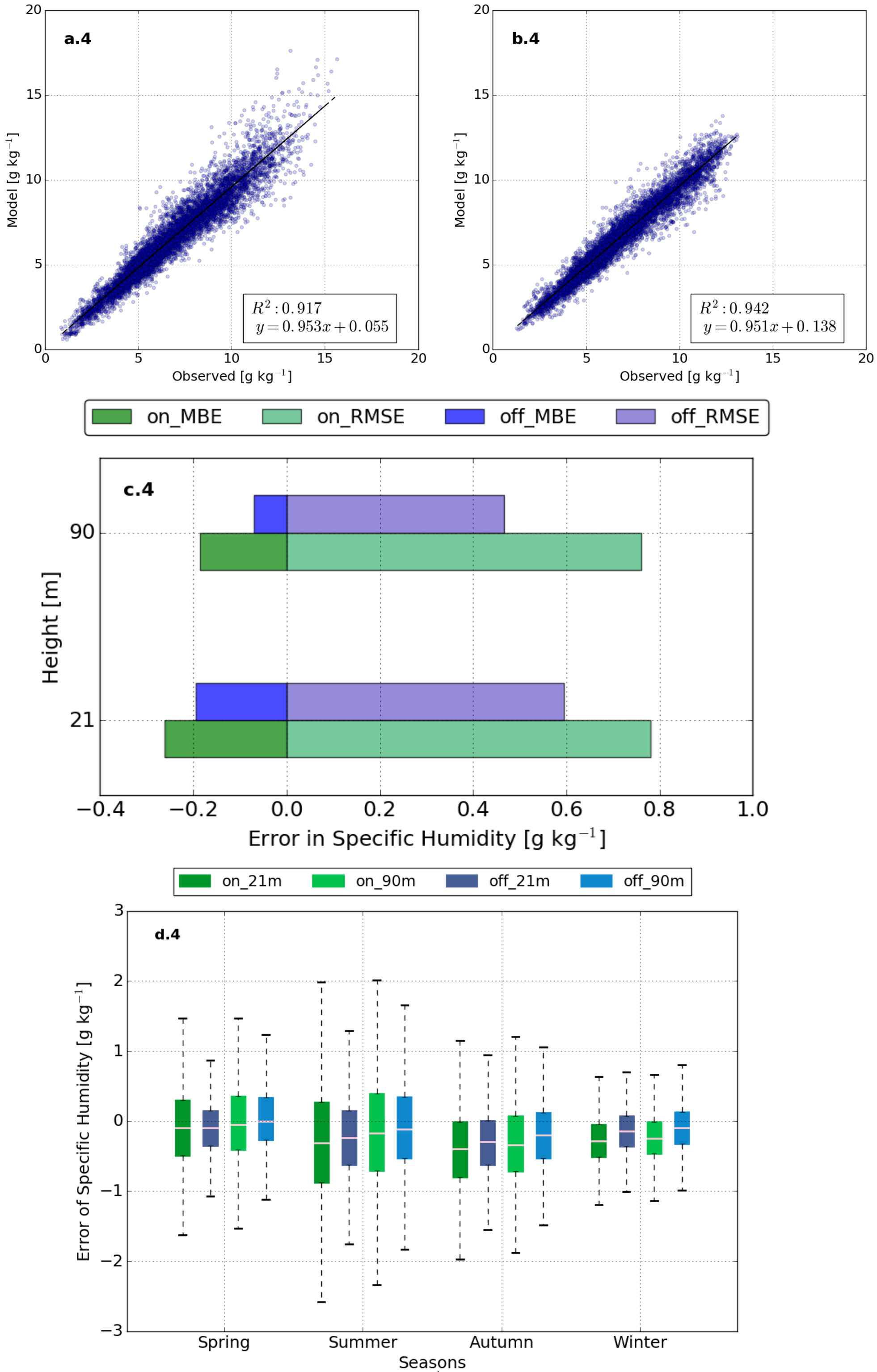

Figure 18: Statistical analysis of specific humidity [g kg^{-1}]. Scatter plots (a and b) of q at 21 m for onshore (a.4) and offshore (b.4) with the observations (x-axis) compared with the model output (y-axis). Bar-chart (c.4) with the bias (MBE) and the root mean square error (RMSE) (x-axis), for onshore (green) and offshore (blue) at heights (y-axis) 21 and 90 m. The darker shade indicates the bias and the pale colour indicates the RMSE. Box-plot (d.4) of the seasonal errors of onshore (green) and offshore (blue) for heights 21 and 90 m, the lighter the shade of the colour the higher the altitude. The pink line indicates the median. The seasons are determined by the meteorlogical seasons: Spring = MAM, Summer = JJA, Autumn = SON, and Winter = DJF.

In Section 3.1.2 we analysed the relationship between θ and q. The model results for q are similar to those of θ, with the overall model performance being better for offshore than onshore. Due to the homogeneous conditions offshore. Previously the results of Figures 16 a.3 and b.3 indicate that, as the temperature increases the scatter becomes much larger. In Figures 18 a.4 and b.4, dense scatter is evident from 0 to 12 g kg^{-1} and a larger spread is seen beyond 12 g kg^{-1}. This is especially noticeable onshore. A reason for this deviation may be due to the large role of entrainment onshore (Figure 9D). The observational data of temperature and specific humidity correlate well with the model.

Once again, the bias and the RMSE of q indicate similar results to θ (Figure 18c.4). The model underestimates the true value of the observations (similar to Figure 16c.3). This is again much greater onshore (- 0.3 g kg^{-1}). The RMSE illustrates that the model represents offshore q at 90 m better than both the measurements at 21 m and the observations onshore. The model has difficulty in representing the seasonal cycles of q (Figure 18d.4). The model is able to represent q in winter much more promisingly than in summer (for both onshore and offshore sites). As heights increase the model results become more reliable. The model has difficulty producing accurate results from spring to summer and from summer to autumn. This is further explored in Figure 19.

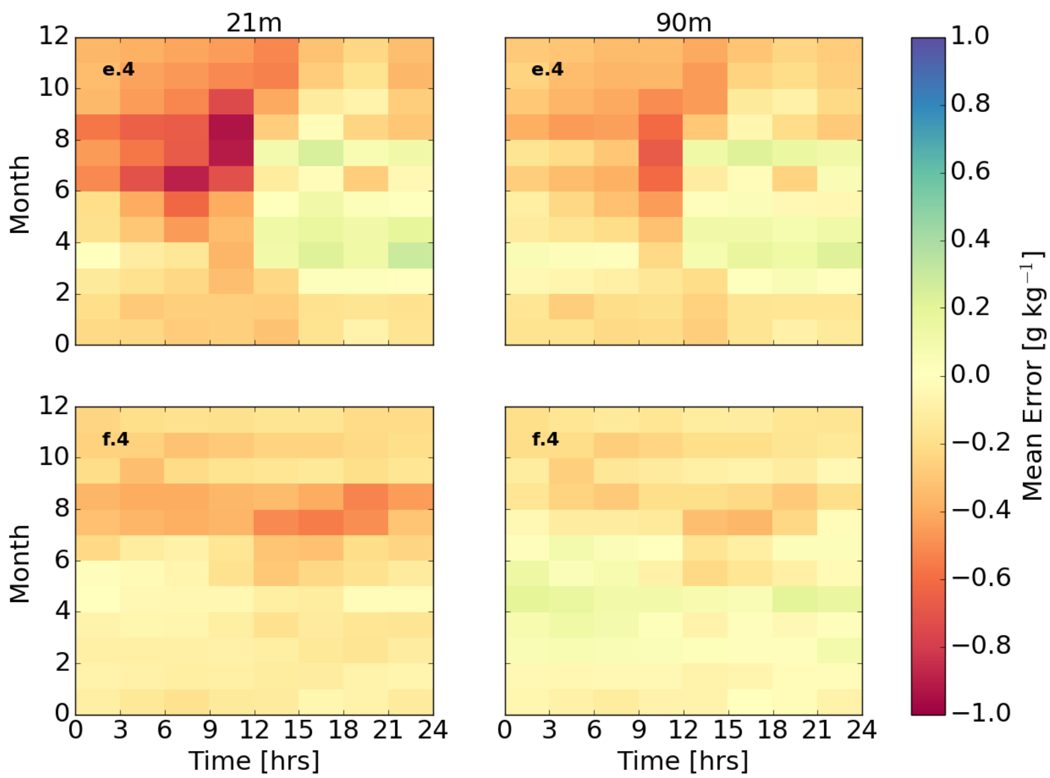

Figure 19: Average diurnal (x-axis) and seasonal (y-axis) cycles of the mean error in specifc humidity [g kg^{-1}] at 21 and 90 m onshore (e.4) and offshore (f.4). The error ranges between -1 (red) and 1 (blue), where red indicates an underestimation of q, and blue indicates an overestimation of q.

At all heights and in both locations, q is underestimated during the transition from summer to autumn (Figure 19). Figure 19e.4 shows a strong relationship onshore at both 21 and 90 m due to the increase in mixing between the altitudes (as discussed in 3.1). During summer months, the model produces slightly dry conditions at 21 m and damp conditions at 90 m offshore. It is possible that the model presumes that there is no change in q with height offshore which is the case as $q90 < q21$ (Figure 9G).

Bengtsson et al. (2017) claims that the cold and moist biases are related to surface and physiography issues. To examine these relations we look at the surface fluxes onshore. Consequently, the underestimation of q during the transitions (Figure 19e.4) may be due to the underestimation of the LE flux. These fluxes are further explored for onshore in Figure 20.

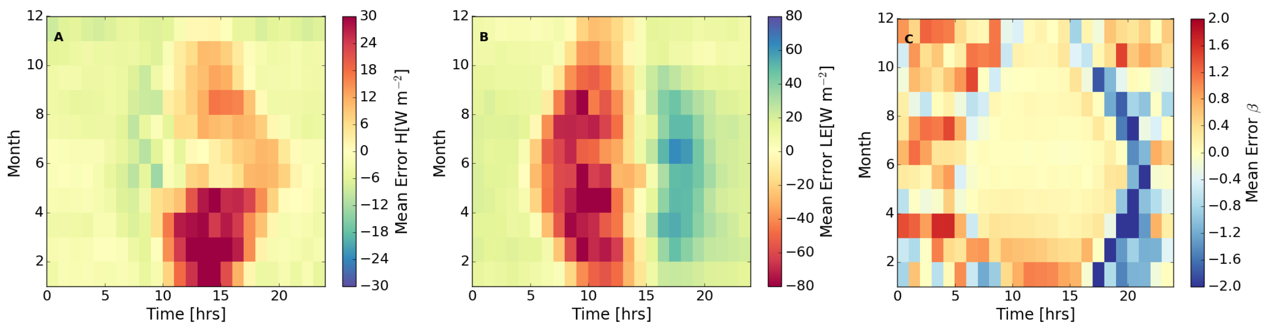

Figure 20: Onshore: Average diurnal (x-axis) and seasonal (y-axis) cycles of the mean error (model - observations) of (A) the sensible heat flux (H) [W m^2], (B) the latent heat flux (LE) [W m^2] and (C) Bowen Ratio ($\beta = H/LE$).

It is observed from Figure 20A that the diurnal cycle of H is overestimated by $\sim$18 W m^{-2}, reaching maximum mean errors of 30 W m^{-2} during the first half of the year. This illustrates that the postulation of the cold bias of Figure 17e.3 being caused by the underestimation of H is inaccurate. However, the assumption that LE impacts the model's ability to predict q is more accurate. The model error is -1 g kg^{-1} during the morning period (Figure 19e.4) and 0.4 g kg^{-1} in the latter half of the day. This relationship is evident in Figure 20B where there is too little surface evaporation ($LE \approx$-40 to -80 W m^{-2}) during the morning period and is overestimated by 40 W m^{-2} after 15:00. This occurs most strongly in summer months where SW$_{in}$ is strong due to small incidence angle creating vigorous turbulence and stronger convection. Although the patterns between q and LE are similar, the error between the model and the observations is large. Furthermore, the Bowen ratio is large where the model overestimates H and underestimates LE (Figure 20C) As explained in section 2.2. Therefore, we can conclude that the surface fluxes may not be the determining factor of the results for θ and q. Instead, the turbulence scheme may have the strongest influence on the variables within the model (Sandu et al., 2013; Muñoz-Esparza et al., 2014).

3.2.3 Discussion of the HARMONIE Model

The HARMONIE model output produced wind speed values accurately with correlation coefficient values of R$^2\approx$0.8 and RMSE$\approx$1.5$-$2 m s^{-1} onshore and offshore. Over land we noted that wind is better represented, with wind speed at 100 m giving RMSE$\approx$1.7 m s^{-1} onshore and 2.3 m s^{-1} offshore. With regards to wind direction, the seasonal cycle of wind direction is more accurately represented onshore, with median values of wind direction error being closer to 0°, and overestimations by the model were observed offshore (median values ranging from 5-10°). However, both θ and q are better reported over the North Sea, with RMSE$\approx$1.6 K and 0.8 g kg^{-1} offshore and 1.2 K and 0.5 g kg^{-1} onshore. From all results it can be concluded that although the error is rather small the spread is substantially large.

HARMONIE represents onshore wind better than offshore wind. This could be a result of the lack of offshore observational input data assimilated, as opposed to the more validated observations found over land. From this hypothesis one could expect that θ and q would be more accurately defined onshore. However, this is not the case. Over the North Sea the model presents more accurate values of θ and q as a result of fewer interactions between the surface and the atmosphere, as opposed to the more complex relations observed over land (see Section 3.1).

Many studies of NWP models have reproduced similar results for errors in wind speed and direction. Kalverla et al. (2018) found that even in short-term runs (2012-2015), wind speed over the North Sea was underestimated by HARMONIE, with a bias of 0.5 m s^{-1} and standard deviation (σ) of < 2 m s^{-1}. For our study wind speed produced $\sigma \approx$1.9-2.3 m s^{-1} (Appendix Table B.1). However the bias offshore is underestimated and smaller than the results found by Kalverla et al. (2018). This indicates that the model results do in fact deviate slightly over a longer run. Brown et al. (2008) found that onshore wind speeds have a bias of 0.4 m s^{-1} which is $\sim$0.3 m s^{-1} larger then the bias produced by HARMONIE. Comparable to our study, Sharp et al. (2015) found that the Climate Forecast System Reanalysis (CFSR) model presented larger RMSE values offshore than onshore, and a smaller bias. They put this down to offshore having more homogeneous conditions.

In the comparison of onshore and offshore wind speed (Figure 14c.1), it is observed that HARMONIE better reproduces areas of reduced drag – i.e. smooth surface conditions at 27 m offshore, and high altitudes (200 m) of geostrophic flow onshore. The inability of the model to represent friction can impact the representation of wind speed and further influence the model interpretation of the turning of the wind (as seen in Figure 8). Kalverla et al. (2018) noted that HARMONIE produced a bias of 10° over the North Sea. This bias is reproduced in Figure 15d.2 during autumn and winter months. However, the spread of error in wind direction is much larger in spring and summer due to the estimation of stability within these months. Many studies (Brown et al., 2005; Svensson and Holtslag, 2009; Sandu et al., 2013; Muñoz-Esparza et al., 2014) have suggested that errors in boundary layer stability have a significant impact on the valid reproduction of wind. Under stable stratified conditions, HARMONIE produces poor results (Kalverla et al., 2018). However, θ and q seem to be a more accurate fit offshore over a longer run then on a shorter time scale. Nevertheless, the stability of the boundary layer needs to be properly assessed within the model. This is evident especially over land where 55% of observations indicate stable conditions, where errors in θ and q are larger (Figures 16 and 18).

A procedure to improve the accuracy of stable conditions within the model is the enhancement of turbulent diffusion in stable conditions (Sandu et al., 2013). This is especially necessary in cases where low level jets are too weak, near surface ageostrophic wind angles are too small and there is an overall underestimation of the turning of wind (Brown et al., 2005; Svensson and Holtslag, 2009). By increasing the turbulent diffusion, the cold biases evident in Figure 17e.3 can be reduce. Cooling as a result of radiative loss at the surface causes near surface temperature to drop and so the cold bias is reduced (Sandu et al., 2013). This increase in diffusion also causes more drag at the surface which maintains the turbulent mixing within the boundary layer (Sandu et al., 2013). This would otherwise impact near surface wind, temperature and specific humidity (Brown et al., 2005).

We suggest evaluating cases of stability demonstrated by the model run depending on particular wind direction as studied by Holtslag (1984) as well as storm events which can be compared with Baas et al. (2016). Additionally, cases of clear, cloudy and fog conditions should be analysed as these impact the stability and growth of the boundary layer (Duynkerke, 1999; Bony and Dufresne, 2005). This can further impact the efficiency of the wind turbine. Furthermore, within this type of model configuration, it is necessary to analyse the model's performance in relation to anomalous wind events, defined by Kalverla et al. (2017) such as low level jets, wind gusts, wind ramps etc. These events impact the load of the turbine and at times can cause total destruction of the turbine. Therefore it is essential for the model to be able to forecast such events.

We propose that the model is run interrupted and reassessed during specific time intervals. Their outputs could then be concatenated to produce the overall 10-year run. This may reduce the deviations of the model which are not climatologically correct, and therefore decrease the overall errors.

4 Conclusions

We presented a comparative study of onshore and offshore boundary layers in the HARMONIE model for the purpose of wind energy. To do so the study was divided into two sections. We first analysed observations for onshore and offshore locations in the Netherlands. The observational sites included: the onshore location of Cabauw representing mid-latitude flat grasslands, and the offshore IJmuiden meteomast located 85 km from the Dutch coast between the years of 2012 and 2014. Wind speed, direction, potential temperature and specific humidity were analysed alongside latent and sensible heat fluxes. IJmuiden experiences more homogeneous conditions at the surface and hence exhibits less wind shear, thus enhancing the amount of energy produced by the turbine. Furthermore less wind shear leads to smaller loads on the turbine blades.

The latter half of this paper focused on the statistical validation of the continuous 10-year run of the HARMONIE model using the observations from the previous study. The HARMONIE model is a NWP model used for short-term weather forecasting in many meteorological agencies in Europe, including the wind energy sector. The run itself is a downscaled product of the ERA-Interim data from 80 km to a more refined scale of 2.5 km. This evaluation included the study of wind speed, direction and stability by looking at potential temperature and specific humidity.

Wind speed and and wind direction were better represented at Cabauw, with biases ranging between -0.1 to 0.1 m s^{-1} and -2 to 1.8°, respectively. Surprisingly, the biases in potential temperature and specific humidity were smaller for IJmuiden with values of -0.09 K and -0.2 g kg^{-1}, respectively. In all cases, although the bias seemed rather small the spread in the errors was large, with RMSE values ranging from 1.2 to 2.3 m s^{-1} for both onshore and offshore locations.

Most importantly these findings relate to the fact that the model has difficulties in representing situations involving entrainment and stable conditions. This form of run should be evaluated further, especially with regards to anomalous wind events. These finding are important to keep in mind for producing accurate meteorological models to represent onshore and offshore locations for the wind energy industry.

5 Acknowledgements

I would like to convey my sincere gratitude to my supervisor Peter Kalverla MSc. Who always devoted time to guiding and helping me when necessary. I benefited through countless support in the form of python codes, meteorological explanations, reassurance and motivation. Without him and his critical feedback I would not have gained the insights into the topic and the process of writing a thesis. I would also like to express my gratitude to my second supervisor Dr. Ir. Gert-Jan Steeneveld, who I am indebted to for his very valuable comments on this thesis.

I would also like to acknowledge Leo Kroon and Prof. Dr. AAM (Bert) Holtslag of the Meteorology and Air Quality department who encouraged and provided me with the opportunity to work on the topic and under the supervision of such incredible people. Furthermore I would like thank Andreas Sterl for providing the HARMONIE output data addressed in this study.

Of course I must express my very profound gratitude to my family and friends for providing me with unfailing support, continuous encouragement and humour throughout my years of study and through the process of researching and writing this thesis. This accomplishment would not have been possible without them.

References

Baas, P., F. Bosveld, and G. Burgers (2016). The impact of atmospheric stability on the near-surface wind over sea in storm conditions. *Wind Energy 19*(2), 187–198.

Beljaars, A. and F. Bosveld (1997). Cabauw data for the validation of land surface parameterization schemes. *Journal of climate 10*(6), 1172–1193.

Bengtsson, L., U. Andrae, T. Aspelien, Y. Batrak, J. Calvo, W. de Rooy, E. Gleeson, B. Hansen-Sass, M. Homleid, M. Hortal, et al. (2017). The harmonie–arome model configuration in the aladin–hirlam nwp system. *Monthly Weather Review 145*(5), 1919–1935.

Bony, S. and J.-L. Dufresne (2005). Marine boundary layer clouds at the heart of tropical cloud feedback uncertainties in climate models. *Geophysical Research Letters 32*(20).

Bosveld, F. (2010). Observering the surface energy budget at cabauw: A status report. *Triennial Scientific Report 2007-2009*, 15.

Bowen, I. S. (1926). The ratio of heat losses by conduction and by evaporation from any water surface. *Physical review 27*(6), 779.

Brown, A., R. Beare, J. Edwards, A. Lock, S. Keogh, S. Milton, and D. Walters (2008). Upgrades to the boundary-layer scheme in the met office numerical weather prediction model. *Boundary-layer meteorology 128*(1), 117–132.

Brown, A., A. Beljaars, H. Hersbach, A. Hollingsworth, M. Miller, and D. Vasiljevic (2005). Wind turning across the marine atmospheric boundary layer. *Quarterly Journal of the Royal Meteorological Society 131*(607), 1233–1250.

Chai, T. and R. R. Draxler (2014). Root mean square error (rmse) or mean absolute error (mae)?– arguments against avoiding rmse in the literature. *Geoscientific model development 7*(3), 1247–1250.

Chen, Y., H. Li, K. Jin, and Q. Song (2013). Wind farm layout optimization using genetic algorithm with different hub height wind turbines. *Energy Conversion and Management 70*, 56–65.

Coelingh, J., A. Van Wijk, and A. Holtslag (1996). Analysis of wind speed observations over the north sea. *Journal of Wind Engineering and Industrial Aerodynamics 61*(1), 51–69.

de Roode, S. R., F. C. Bosveld, and P. S. Kroon (2010). Dew formation, eddy-correlation latent heat fluxes, and the surface energy imbalance at cabauw during stable conditions. *Boundary-layer meteorology 135*(3), 369–383.

Dee, D. P., S. Uppala, A. Simmons, P. Berrisford, P. Poli, S. Kobayashi, U. Andrae, M. Balmaseda, G. Balsamo, P. Bauer, et al. (2011). The era-interim reanalysis: Configuration and performance of the data assimilation system. *Quarterly Journal of the royal meteorological society 137*(656), 553–597.

Dörenkämper, M., B. Witha, G. Steinfeld, D. Heinemann, and M. Kühn (2015). The impact of stable atmospheric boundary layers on wind-turbine wakes within offshore wind farms. *Journal of Wind Engineering and Industrial Aerodynamics 144*, 146–153.

Draxl, C., B. Hodge, A. Clifton, and J. McCaa (2015). Overview and meteorological validation of the wind integration national dataset toolkit. *NREL/TP-5000-61740. Golden (CO): National Renewable Energy Laboratory (forthcoming), Tech. Rep.*.

Duynkerke, P. G. (1999). Turbulence, radiation and fog in dutch stable boundary layers. *Boundary-Layer Meteorology 90*(3), 447–477.

Edenhofer, O., R. Pichs-Madruga, Y. Sokona, K. Seyboth, S. Kadner, T. Zwickel, P. Eickemeier, G. Hansen, S. Schlömer, C. von Stechow, et al. (2011). *Renewable energy sources and climate change mitigation: Special report of the intergovernmental panel on climate change*. Cambridge University Press.

Emeis, S. (2014). Current issues in wind energy meteorology. *Meteorological Applications 21*(4), 803–819.

Engström, S., T. Lyrner, M. Hassanzadeh, T. Stalin, and J. Johansson (2010). Tall towers for large wind turbines. *Report from Vindforsk project 342*, 50.

Flamant, C., J. Pelon, D. Hauser, C. Quentin, W. M. Drennan, F. Gohin, B. Chapron, and J. Gourrion (2003). Analysis of surface wind and roughness length evolution with fetch using a combination of airborne lidar and radar measurements. *Journal of Geophysical Research: Oceans 108*(C3).

Gönnert, G. and K. Sossidi (2011). A new approach to calculate extreme storm surges: analysing the interaction of storm surge components. *WIT Transactions on Ecology and the Environment 149*, 139–150.

González, J. S. and R. Lacal-Arántegui (2016). A review of regulatory framework for wind energy in european union countries: current state and expected developments. *Renewable and Sustainable Energy Reviews 56*, 588–602.

Henderson, A. R., C. Morgan, B. Smith, H. C. Sørensen, R. J. Barthelmie, and B. Boesmans (2003). Offshore wind energy in europe—a review of the state-of-the-art. *Wind energy 6*(1), 35–52.

Holtslag, A. (1984). Estimates of diabatic wind speed profiles from near-surface weather observations. *Boundary-Layer Meteorology 29*(3), 225–250.

Hsu, S. (1980). On the correction of land-based wind measurements for oceanographic applications. In *Coastal Engineering 1980*, pp. 708–724.

Hsu, S. (1986). Correction of land-based wind data for offshore applications: a further evaluation. *Journal of physical oceanography 16*(2), 390–394.

Hsu, S.-A. (2013). *Coastal meteorology*. Elsevier. ISBN: 978-00-805-0215-1.

Kaldellis, J. and M. Kapsali (2013). Shifting towards offshore wind energy—recent activity and future development. *Energy Policy 53*, 136–148.

Kalverla, P. C., G.-J. Steeneveld, R. J. Ronda, and A. A. Holtslag (2017). An observational climatology of anomalous wind events at offshore meteomast ijmuiden (north sea). *Journal of Wind Engineering and Industrial Aerodynamics 165*, 86–99.

Kalverla, P. C., G.-J. Steeneveld, R. J. Ronda, and A. A. Holtslag (2018). A statistical evaluation of three mainstream numerical weather prediction models against the ijmuiden observations at the north sea. *submitted to Wind Energy*.

Landberg, L. (2015). *Meteorology for wind energy: an introduction*. John Wiley & Sons.

Lee, J., W. Cho, and K.-S. Lee. Optimization of the hub height of a wind turbine. *Journal of Industrial and Intelligent Information Vol*, 275–279.

Moene, A. F. and J. C. Van Dam (2014). *Transport in the atmosphere-vegetation-soil continuum.* Cambridge University Press.

Muñoz-Esparza, D., B. Kosović, J. Mirocha, and J. van Beeck (2014). Bridging the transition from mesoscale to microscale turbulence in numerical weather prediction models. *Boundary-layer meteorology 153*(3), 409–440.

Murphy, A. H. (1988). Skill scores based on the mean square error and their relationships to the correlation coefficient. *Monthly weather review 116*(12), 2417–2424.

Nurmi, P. (2003). Recommendations on the verification of local weather forecasts.

Peña, A., R. Floors, A. Sathe, S.-E. Gryning, R. Wagner, M. S. Courtney, X. G. Larsén, A. N. Hahmann, and C. B. Hasager (2016). Ten years of boundary-layer and wind-power meteorology at høvsøre, denmark. *Boundary-Layer Meteorology 158*(1), 1–26.

Porté-Agel, F., H. Lu, and Y.-T. Wu (2014). Interaction between large wind farms and the atmospheric boundary layer. *Procedia Iutam 10*, 307–318.

Poveda, J. M. and D. Wouters. *Wind Measurements at Meteorological Mast IJmuiden.*

Rodrigues, S., C. Restrepo, E. Kontos, R. T. Pinto, and P. Bauer (2015). Trends of offshore wind projects. *Renewable and Sustainable Energy Reviews 49*, 1114–1135.

Sandu, I., A. Beljaars, P. Bechtold, T. Mauritsen, and G. Balsamo (2013). Why is it so difficult to represent stably stratified conditions in numerical weather prediction (nwp) models? *Journal of Advances in Modeling Earth Systems 5*(2), 117–133.

Sathe, A. (2010). Atmospheric stability and wind profile climatology over the north sea: Case study at egmond aan zee. In *3rd EWEA Conference-Torque 2010: The Science of making Torque from Wind, Heraklion, Crete, Greece, 28-30 June 2010.* European Wind Energy Association.

Sharp, E., P. Dodds, M. Barrett, and C. Spataru (2015). Evaluating the accuracy of cfsr reanalysis hourly wind speed forecasts for the uk, using in situ measurements and geographical information. *Renewable Energy 77*, 527–538.

Shen, X., C. Zhou, and X. Fu (2018). Study of time and meteorological characteristics of wind speed correlation in flat terrains based on operation data. *Energies 11*(1), 219.

Smits, A., A. Klein Tank, and G. Können (2005). Trends in storminess over the netherlands, 1962–2002. *International Journal of Climatology 25*(10), 1331–1344.

Steeneveld, G., A. Holtslag, and H. DeBruin (2005). Fluxes and gradients in the convective surface layer and the possible role of boundary-layer depth and entrainment flux. *Boundary-layer meteorology 116*(2), 237–252.

Sterl, A., A. M. Bakker, H. W. van den Brink, R. Haarsma, A. Stepek, I. L. Wijnant, and R. C. de Winter (2015). Large-scale winds in the southern north sea region: the wind part of the knmi'14 climate change scenarios. *Environmental Research Letters 10*(3), 035004.

Storm, B., J. Dudhia, S. Basu, A. Swift, and I. Giammanco (2009). Evaluation of the weather research and forecasting model on forecasting low-level jets: Implications for wind energy. *Wind Energy 12*(1), 81–90.

Stull, R. (2000). *Meteorology for scientists and engineers.* Brooks/Cole.

Svensson, G. and A. Holtslag (2009). Modelling the turning of wind with height in the stable boundary layer. *Boundary-Layer Meteorol 132*, 261–277.

Van den Berg, G. (2008). Wind turbine power and sound in relation to atmospheric stability. *Wind Energy 11*(2), 151–169.

van den Brink, H. W. and F. C. Bosveld (2017). Bringing modelled and observed surface winds together. *International Journal of Climatology 37*(14), 4783–4790.

van der Brink, H., P. Baas, and G. Burgers (2013). Towards an approved model set-up for harmonie contribution to wp 1 of the sbw-hb wind modelling project. Technical report, Technical report, KNMI.

Van Ulden, A. and J. Wieringa (1996). Atmospheric boundary layer research at cabauw. In *Boundary-Layer Meteorology 25th Anniversary Volume, 1970–1995*, pp. 39–69. Springer.

Van Wijk, A., A. Beljaars, A. Holtslag, and W. Turkenburg (1990). Evaluation of stability corrections in wind speed profiles over the north sea. *Journal of Wind Engineering and Industrial Aerodynamics 33*(3), 551–566.

Verkaik, J. and A. Holtslag (2007). Wind profiles, momentum fluxes and roughness lengths at cabauw revisited. *Boundary-layer meteorology 122*(3), 701–719.

Vilà-Guerau de Arellano, J., C. C. Van Heerwaarden, B. J. Van Stratum, and K. Van Den Dries (2015). *Atmospheric boundary layer: Integrating air chemistry and land interactions*. Cambridge University Press.

Wallace, J. M. and P. V. Hobbs (2006). *Atmospheric science: an introductory survey*, Volume 92. Elsevier.

Weisse, R. and H. Von Storch (2010). *Marine climate and climate change: storms, wind waves and storm surges*. Springer Science & Business Media.

Weisse, R., H. von Storch, H. D. Niemeyer, and H. Knaack (2012). Changing north sea storm surge climate: An increasing hazard? *Ocean & coastal management 68*, 58–68.

Werkhoven, E. and J. Verhoef (2012). Offshore meteorological mast ijmuiden–abstract of instrumentation report. *ECN-Wind Memo-12 10*.

Wikipedia (2005, August). Meetmast cabauw.

WindEurope (2018). Wind in power 2017 - annual combined onshore and offshore wind energy statistics.

Yu, X. and L. Yan (2017). High humidity aerodynamic effects study on offshore wind turbine airfoil/blade performance through cfd analysis. In *ASME Turbo Expo 2017: Turbomachinery Technical Conference and Exposition*, pp. V009T49A001–V009T49A001. American Society of Mechanical Engineers.

A Climatological Variable Calculations

A.1 Potential Temperature and Specific Humidity

Wallace and Hobbs (2006), define potential temperature (θ), as the temperature that an air parcel has if it is dried adiabatically from its current pressure and temperature to a standard pressure, (i.e. the temperature that a parcel could have if it moves through a dry atmosphere to a pressure of 101.3 kPa). The potential temperature is calculated using the following equation:

$$\theta = T \cdot (\frac{p_0}{p})^{\frac{R_d}{c_p}}, \tag{A.1}$$

in which T is air temperature [K], p_0 is the standard pressure of 100 kPa, R_d is the specific gas constant for dry air with a value of 287 J K^{-1} $kg^{-}1$, and c_p is the specific heat of dry air at a constant pressure of 1004 J K^{-1} kg^{-1}. The pressure of air (p) is calculated from $p = p_0 \exp(\frac{-z}{H_s})$, where H_s is 7500 m and z is the height. Combining these two equations the potential temperature can be re-written as:

$$\theta = T \cdot (\exp(\frac{-z}{H}))^{\frac{-R_d}{c_p}}, \tag{A.2}$$

whereby specific humidity (q) is the mass of water vapour in a unit mass of dry air (Wallace and Hobbs, 2006) measured in kg/kg. q is calculated using the relationship with the mixing ratio (w), such that $q = w$. Therefore, the following equation is used:

$$q = \frac{e}{p} \cdot \epsilon, \tag{A.3}$$

where $\epsilon = 0.622$ and e is the vapour pressure [Pa]. e is derived from the dew point temperature (T_D) through the use of the Empirical Tetens equation (Stull, 2000):

$$e = 0.611 \cdot \exp(\frac{17.2694 \cdot (273.16 - T_D)}{T_D - 35.86}). \tag{A.4}$$

A.2 Stability

Wind speed, turbulence and stability contribute and can be determined by the logarithmic wind profile:

$$U(z) = \frac{u_*}{\kappa} \cdot \ln \frac{z}{z_0} \tag{A.5}$$

Where U(z) is the wind speed at height z, $u*$ is the friction/shear velocity, κ is the von karman constant (∼0.4) and z_0 is the roughness length (Holtslag, 1984). For stability effects to be taken into account, equation A.5 is modified by the addition of the stability function Ψ resulting in the diabatic wind profile (Coelingh et al., 1996):

$$U(z) = \frac{u_*}{\kappa} \cdot (\ln \frac{z}{z_0} - \Psi(\frac{z}{L})) \tag{A.6}$$

Stability is taken into account by the use of the Obukhov length (L) from the Monin-Obukhov Stability Theory (MOST). However as many of the variables of L are not measured in the data, the Bulk-Richardson number Ri_b is used in the estimation of stable ($0 < Ri_b < 0.2$) and unstable conditions (Moene and Van Dam, 2014; Wallace and Hobbs, 2006). To make use of this theory, the following conditions were used:

- The temperature and wind speed are measured at two heights,
- The ratio between these heights is less than 6.
- The effect of humidity on buoyancy is ignored (Moene and Van Dam, 2014).

The flux measurements are taken close to the surface. Therefore, it was necessary to choose heights that are both close to the surface and obey the second condition (having a ratio in heights less than 6). Thus, for the case at Cabauw we chose heights of 10 m and 40 m.

In determining the flux-gradient relationships, the following equations from Moene and Van Dam (2014) were used:
For unstable conditions:

$$\frac{H}{\rho \cdot c_p} = \frac{-k^2 \cdot \Delta\overline{\theta} \cdot \Delta\overline{u}}{[\ln(\frac{z_2}{z_1})]^2} \cdot (1 - 16 \cdot Ri_{b*})^{\frac{3}{4}}, \tag{A.7}$$

with H in W m^{-2}, ρ is the density of air at sea level 1.25 kg m^{-3}.

$$\frac{LE}{\rho \cdot L_v} = \frac{-k^2 \cdot \Delta\overline{q} \cdot \Delta\overline{u}}{[\ln(\frac{z_2}{z_1})]^2} \cdot (1 - 16 \cdot Ri_{b*})^{\frac{3}{4}}, \tag{A.8}$$

(LE) is measured in W m^{-2}, and L_v as the latent heat for vaporization at 0^oC. The equivalent Bulk Richardson number (Ri_{b*}) is determined from the equation:

$$Ri_{b*} = \sqrt{z_2 \cdot z_1} \cdot \ln(\frac{z_2}{z_1}) \cdot \frac{g}{T_v} \cdot \frac{\Delta\overline{\theta}}{(\Delta\overline{u})^2} \tag{A.9}$$

.
Similarly, for stable conditions, where $0 < Ri_b < 0.2$:

$$\frac{H}{\rho \cdot c_p} = \frac{-k^2 \cdot \Delta\overline{\theta} \cdot \Delta\overline{u}}{[\ln(\frac{z_2}{z_1})]^2} \cdot (1 - 5 \cdot Ri_b)^2, \tag{A.10}$$

$$\frac{LE}{\rho \cdot L_v} = \frac{-k^2 \cdot \Delta\overline{q} \cdot \Delta\overline{u}}{[\ln(\frac{z_2}{z_1})]^2} \cdot (1 - 5 \cdot Ri_b)^2. \tag{A.11}$$

The Bulk Richardson number Ri_b is then calculated using the equation:

$$Ri_b = \frac{g}{T_v} \cdot \frac{\Delta\overline{\theta}}{\Delta\overline{u}^2} \cdot \Delta z, \tag{A.12}$$

in this case $\Delta z = (z_2 - z_1)$.

A.3 Preliminary Results for Latent and Sensible Heat Fluxes

This section shows the results of the calculation of H and LE from Appendix A.2 for the observations from Cabauw. The heights selected for this study were 10 m and 40 m as these were closest to the surface and obeyed the conditions for this approach.

For both cases of H (Figure A.1) and LE (Figure A.2) it is evident that this approach does not achieve accurate results quantitatively, with R^2 values of 0.3 for H and 0.06 for LE.

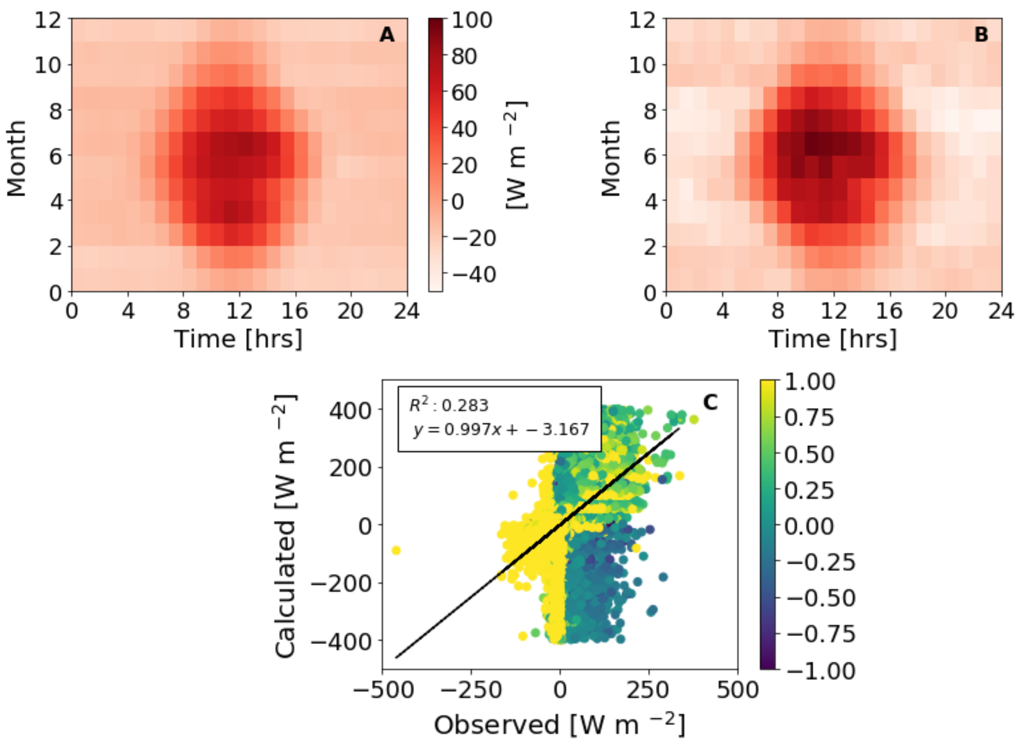

Figure A.1: Diurnal (x-axis) and seasonal (y-axis) cycles of the sensible heat flux [W m^{-2}], for onshore from the observations (A) and calculated (B) using the equations from Appendix A.2. C indicates the regression of the scatter plot of the calculated H versus the observed H, giving information on the R^2 and the equation of the line. The colour bar denotes the change in wind speed ΔU.

Figure A.1A and Figure A.1B indicate that the model represents the diurnal cycle rather accurately with maximum values of ∼90 W m^2 in both the observed and calculated H increasing at 05:00 and decreasing at 18:00. However during night time hours in the summer the calculated H ≈-40 W m^2 (Figure A.1B) as opposed to observational values H ≈10 W m^2 seen in Figure A.1A.

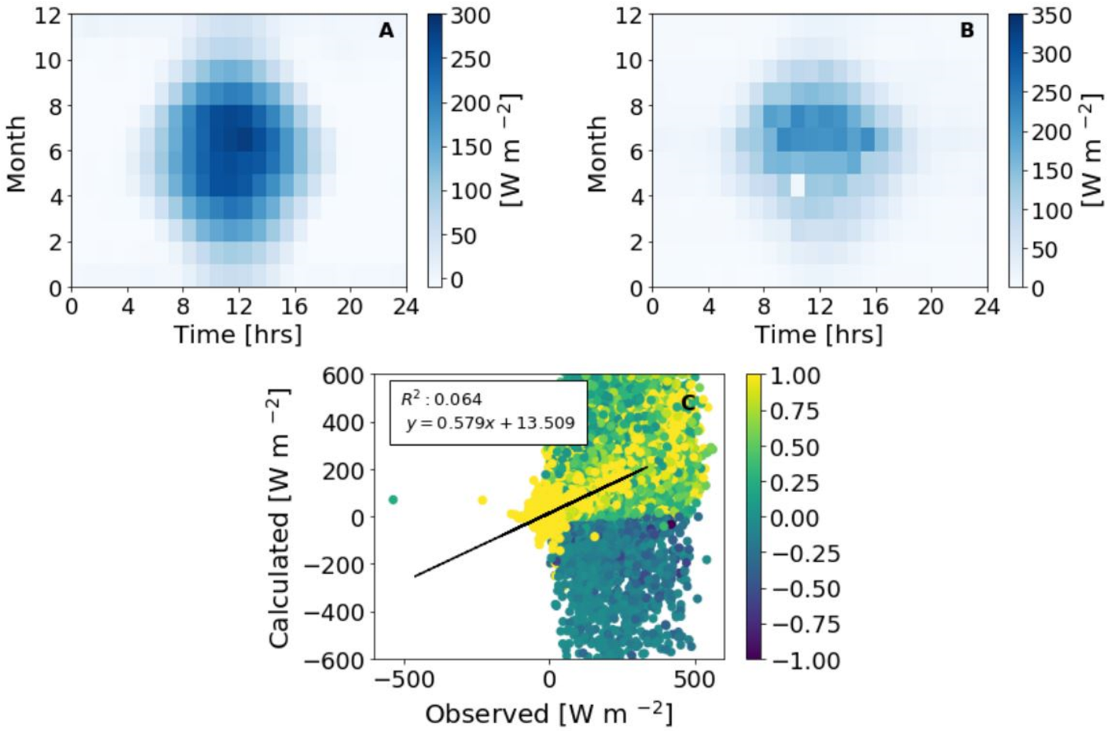

Figure A.2: Diurnal (x-axis) and seasonal (y-axis) cycles of the latent heat flux [W m^{-2}], for onshore observations (A) and calculated (B) using the equations from Appendix A.2. C indicates the regression of the scatter plot of the calculated LE versus the observed LE, giving information on the R^2 and the equation of the line. The colour bar denotes the change in wind speed ΔU.

Figure A.2A and Figure A.2B indicate similar results to those of H. The model represents the diurnal cycle rather accurately, although to a lesser degree than those of previous results (the R^2 value of 0.06). LE does in fact increase from 05:00 and decrease at 18:00 for both calculated and observed values. However, the calculated LE does not depict the substantial amount of moisture that occurs throughout the year with maximum values reaching $\sim$200 W m^2 as opposed to values of $\sim$350 W m^2 that occur in the observations (Figure A.2A).

This method is invalid for Cabauw due to the fact that the model is unable to accurately represent the entrainment that occurs within the observations (Section 3.2). Furthermore this method of calculating the fluxes is not suited to onshore locations as we assume that the effect of humidity on buoyancy is removed. However, Cabauw remains relatively moist, which in turn impacts the buoyancy, and entrainment and moisture have a significant role to play in the boundary layer structure.

B Average Diurnal and Seasonal Cycle of the Bowen Ratio

The error between the model and observational Bowen ratio (β) is briefly introduced in Section 3.2.2 in the discussion of the sensible and latent heat fluxes at Cabauw. This section discusses β for the HARMONIE model output and observational data at Cabauw. For this study we look at the Bowen ratio from the energy balance where $\beta = H/LE$ (Bowen, 1926). As seen in Figure 20C in Section 3.2.2 it is evident that β is too large. H is overestimated as the model underestimates the entrainment that occurs in the observations (Figure 20A). Furthermore, LE is underestimated creating a drier boundary layer, with too little evaporation (Figure 20B). Figure B.1 illustrates the monthly and diurnal cycle of the Bowen ratio for the model and observational output of Cabauw.

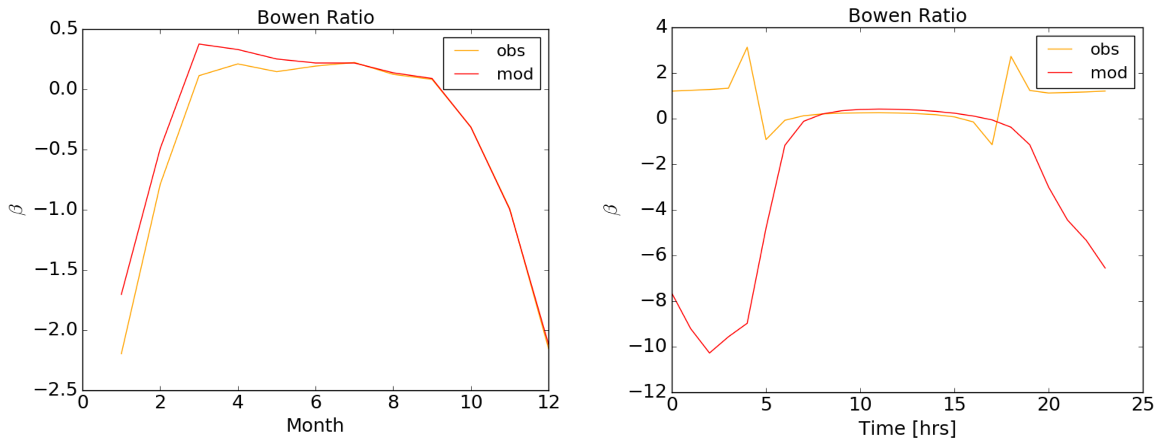

(a) (b)

Figure B.1: Average (a) monthly and (b) diurnal cycle of the Bowen ratio (β) of Cabauw, for observations in orange (obs) and model in red (mod), with time on the x-axis and β on the y-axis

There is a slight overestimation ($\sim$0.3) in the first half of the year, with the model representing more accurate β in the latter half of the year (Figure B.1a). This slight overestimation is due to the model's overestimation of the sensible heat flux during these months (Figure 20A).

Figure B.1b shows the greatest deviation between the model and the observational results of β. This is especially noticeable during the night. This is due to the fact that the model assumes that $LE > 0\ W\ m^{-2}$ at all hours of the day, whereas the observational data indicate slight negative values ($\sim -10\ W\ m^{-2}$). This explains the large negative values between 00:00-05:00, as $H < 0$ and $LE > 0$. This deviation may be a result of the fact that the model assumes closure of the energy balance. However, this is not the case for the observations as discussed in Section 2.2.

C Table Format of Statistical Results

Summary of the error statistics from the results of Section 3.2. For these summaries the mean absolute error has also been included, where:

$$MAE = \frac{1}{n}\sum_{i=1}^{n}|e_i|, \tag{C.1}$$

giving additional information to the error, where the absolute difference between the model and the observations (Chai and Draxler, 2014).

Table C.1: Statistical analysis of the error between the model and the observations with regards to wind speed (wspd) [m s−1] and wind direction (wdir) [°]. The standard deviation (σ), mean bias error (MBE), root mean square error (RMSE) and mean absolute error (MAE) are given for both onshore and offshore conditions at heights of 27, 100 and 200 m.

Location	Height (m)	σ		MBE		RMSE		MAE	
		wspd (m s^{-1})	wdir (^{o})	wspd (m s^{-1})	wdir (^{o})	wspd (m s^{-1})	wdir (^{o})	wspd(m s^{-1})	wdir (^{o})
Onshore	27	1.2854	34.7004	-0.1306	1.8391	1.292	34.749	0.9828	20.1194
	100	1.6531	37.0181	0.1004	-0.5530	1.6561	37.022	1.2607	21.172
	200	1.9993	34.6294	0.0044	-2.1722	1.9992	34.697	1.5255	19.860
Offshore	27	1.9149	35.868	-0.0121	2.5190	1.915	35.9566	1.3998	20.6100
	100	2.2053	35.5492	-0.2194	4.2485	2.2161	35.8022	1.6227	21.1420
	200	2.3374	35.8866	-0.2326	5.6513	2.3488	36.3289	1.7245	21.9469

Table C.2: Statistical analysis of the error between the model and the observations with regards to potential temperature (θ) [K]. The standard deviation (σ), mean bias error (MBE), root mean square error (RMSE) and mean absolute error (MAE) are given for both onshore and offshore conditions at heights of 21 and 90 m.

Location	Height (m)	σ	MBE	RMSE	MAE
Onshore	21	1.459	-0.717	1.626	1.230
	90	1.345	-0.515	1.440	1.062
Offshore	21	1.159	-0.096	1.163	0.903
	90	1.284	-0.077	1.287	0.982

Table C.3: Statistical analysis of the error between the model and the observations with regards to specific humidity (q) [g kg^{-1}]. The standard deviation (σ), mean bias error (MBE), root mean square error (RMSE) and mean absolute error (MAE) are given for both onshore and offshore conditions at heights of 21 and 90 m.

Location	Height (m)	σ	MBE	RMSE	MAE
Onshore	21	0.736	-0.261	0.781	0.580
	90	0.738	-0.185	0.761	0.555
Offshore	21	0.561	-0.194	0.594	0.435
	90	0.653	-0.071	0.466	0.657